NASA TECHNICAL NOTE

NASA TN D-5552

c. 1

TECH LIBRARY KAFB, NM
0132605

NASA TN D-5552

A PERFORMANCE ANALYSIS OF THE OPTICAL-MECHANICAL SCANNER AS AN IMAGING SYSTEM FOR PLANETARY LANDERS

by Friedrich O. Huck and Jules J. Lambiotte, Jr.

Langley Research Center
Langley Station, Hampton, Va.

NATIONAL AERONAUTICS AND SPACE ADMINISTRATION • WASHINGTON, D. C. • DECEMBER 1969

TECH LIBRARY KAFB, NM

0132605

1. **Report No.**
NASA TN D-5552

2. **Government Accession No.**

3. **Recipient's Catalog No.**

4. **Title and Subtitle**
A PERFORMANCE ANALYSIS OF THE OPTICAL-MECHANICAL SCANNER AS AN IMAGING SYSTEM FOR PLANETARY LANDERS

5. **Report Date**
December 1969

6. **Performing Organization Code**

7. **Author(s)**
Friedrich O. Huck and Jules J. Lambiotte, Jr.

8. **Performing Organization Report No.**
L-6864

9. **Performing Organization Name and Address**
NASA Langley Research Center
Hampton, Va. 23365

10. **Work Unit No.**
125-24-05-07-23

11. **Contract or Grant No.**

12. **Sponsoring Agency Name and Address**
National Aeronautics and Space Administration
Washington, D.C. 20546

13. **Type of Report and Period Covered**
Technical Note

14. **Sponsoring Agency Code**

15. **Supplementary Notes**

16. **Abstract**

An analysis is presented of the performance characteristics and trade-off requirements imposed on the optical-mechanical scanner by a planetary-lander configuration. The performance parameters considered are signal-to-noise ratio, angular scanning resolution, tolerance for defect of focus, and video-acquisition rate. Results show how these parameters are interrelated and what trade-offs must be made for a specific mission. A model of the Martian environment used for the preliminary design of the Viking lander is considered.

17. **Key Words** Suggested by Author(s)
Optical-mechanical scanner
Facsimile camera
Planetary lander

18. **Distribution Statement**
Unclassified – Unlimited

19. **Security Classif. (of this report)**
Unclassified

20. **Security Classif. (of this page)**
Unclassified

21. **No. of Pages**
41

22. **Price***
$3.00

*For sale by the Clearinghouse for Federal Scientific and Technical Information
Springfield, Virginia 22151

TABLE OF CONTENTS

A PERFORMANCE ANALYSIS OF THE OPTICAL-MECHANICAL SCANNER AS AN IMAGING SYSTEM FOR PLANETARY LANDERS

By Friedrich O. Huck and Jules J. Lambiotte, Jr.
Langley Research Center

SUMMARY

An analysis is presented of the performance characteristics and trade-off requirements imposed on the optical-mechanical scanner by a planetary-lander configuration. The performance parameters considered are signal-to-noise ratio, angular scanning resolution, tolerance for defect of focus, and video-acquisition rate. Results show how these parameters are interrelated and what trade-offs must be made for a specific mission. A model of the Martian environment used for the preliminary design of the Viking lander is considered.

INTRODUCTION

An optical-mechanical scanner, also called a facsimile camera, is an imaging device which consists basically of a radiometer and a scanning mechanism. The objective lens of the radiometer captures radiation and transmits it through a pinhole to a detector which transforms it into an electrical signal. The pinhole size and distance from the lens determine the instantaneous field of view, or angular scanning resolution. The scanning mechanism provides the line scan, either by a nodding mirror or rotating prism in the object space of the objective lens or by a moving pinhole in its image space. (See ref. 1.) Proper spacing between successive scan lines is provided by the rotation of the complete radiometer and line-scan assembly. Reconstruction of the electrical signal with the aid of synchronous pulses derived from the scanning mechanism produces an image of the surrounding terrain.

Because the optical-mechanical scanner can be made small in size, light in weight, and low in power requirement, it is an attractive candidate for an imaging device for planetary landers. This device has other advantages: Multispectral data can readily be obtained over a wide spectral region; the scanning rate can be adjusted to the data-transmission rate, which allows buffer-free operation; and the surrounding terrain can be surveyed in one frame, which alleviates the data redundancy required to mosaic separate frames.

A major consideration in the design of the optical-mechanical scanner for a lander configuration arises from the continuously varying object distance during each line scan. Because of this variation, the conjugate image plane moves in and out of the pinhole plane causing continuously changing out-of-focus blur. Focus control would be desirable to overcome this problem; but it could, depending on the required accuracy, considerably complicate the scanning mechanism. The continuously varying viewing geometry within each frame also results in the apparent variation of surface radiance and object contrast during each line scan.

A detailed performance analysis of an optical-mechanical scanner for planetary landers has not been published, although this device was used successfully on the Union of Soviet Socialist Republics spacecraft Luna-9 and Luna-13 (refs. 2 to 6) and has also been under development for the National Aeronautics and Space Administration since early 1961 (refs. 7 and 8). Because of the possible selection of this device as an imaging system for the Viking lander, the present study was made to investigate the performance characteristics and trade-off requirements specifically imposed on it by a lander configuration. Other important factors, such as scan linearity, calibration, and video-signal processing, are not considered.

The analysis is introduced with an evaluation of the out-of-focus blur degradation on the performance of the optical-mechanical scanner according to geometrical and physical optics. The amount of radiation captured by the scanner's instantaneous field of view is then derived as a function of the lander viewing geometry, and expressions are given for the signal-to-noise ratio and noise-equivalent radiance for solid-state detectors. Combining the results from the optical and radiometric analyses yields an equation for the image signal-to-noise ratio for objects near the angular scanning resolution, either in or out of focus. Finally, the results of these analyses are used to evaluate performance characteristics and trade-off requirements for this imaging device in the Martian environment.

SYMBOLS

A_D	detector area, meters^2
δA_l	area increment in lens plane, meters^2
δA_o	area increment in object plane, meters^2
a_N	numerical aperture
b	ratio of circular-object radius to scan-element radius (see eq. (4b))

D	lens diameter, meters
D_{λ}^{*}	spectral detectivity of detector, meter-$\sqrt{\text{hertz}}$/watt
$d(u;s)$	lens modulation transfer function (MTF) of defocused optical system
e	electron charge, coulombs
$F(\ )$	spatial distribution
f	lens focal length, meters
$f(\ )$	spatial frequency distribution
g	phase angle, degrees (see fig. 11)
$I(u,v_o)$	normalized fraction of radiation incident on pinhole
$J_n(\ )$	nth order Bessel function, where $n = 0, 1, 2, \ldots$
j,μ,ν,ω	dummy variables
k	spatial frequency, lines/meter
k_x,k_y	spatial-frequency components, lines/meter
L	object-plane distance from lens, meters (see fig. 2)
L_o	in-focus object-plane distance from lens, meters
ΔL	depth of field, meters
l	image-plane distance from lens, meters (see fig. 2)
l_o	pinhole-plane distance from lens, meters (see fig. 2)
Δl	pinhole-plane distance from image plane, meters (see fig. 2)
m	number of binary digits used for encoding shades of gray, bits

N_λ	spectral radiance, watts/meter^2-micrometer-steradian
ΔN_λ	spectral radiance difference, watts/meter^2-micrometer-steradian
$\hat{N}$	unit vector normal to sloped surface
$\hat{N}_o$	unit vector normal to flat surface
$(NEP)_\lambda$	noise-equivalent power, watts
ΔNER	noise-equivalent radiance difference, watts/meter^2-steradian
n	index of refraction (assumed equal to unity herein)
$P(u,v_o;b)$	normalized peak image level of circular object
$P(u,v_o;b,v)$	normalized image distribution of circular object
P_λ	spectral radiant power, watts/micrometer
ΔP_λ	spectral radiance power difference, watts/micrometer
$p(v_o;s)$	pinhole modulation transfer function (MTF)
$Q_{2\mu}(v_o)$	dummy variable defined by equation (8b)
R	radius of circular object, meters (see eq. (4b))
R_o	radius of scan element, meters (see eq. (4a))
r	radial distance from the optical axis, meters
r_o	radius of pinhole, meters (see fig. 3)
Δr	radius of uniform radiation in image space, meters (see fig. 3)
S_λ	solar irradiance above Martian atmosphere, watts/meter^2-micrometer
$S_{\lambda,u}$	solar irradiance at 1.0 astronomical unit (AU), watts/meter^2-micrometer

S/N	average signal-to-rms-noise ratio
$(S/N)_p$	peak signal-to-rms-noise ratio from circular object
s	dimensionless variable for spatial frequency k (see eq. (11))
T	transmission rate, bits/second
t_d	dwell time, seconds
t_f	frame-acquisition time, seconds
u	dimensionless variable for radius Δr (see eq. (5))
v	dimensionless variable for radius r
v_o	dimensionless variable for radius r_o (see eq. (6))
W	video bandwidth, hertz
x,y	spatial dimensions, meters
Y_j	dummy variable, where $j = 1, 2, \ldots$ (see eq. (8e))
α	object slope, degrees
β	angular scanning resolution, or instantaneous field of view, degrees or radians (see fig. 2)
γ	dummy variable
ϵ	angle between emitted radiation and normal to sloped surface, degrees (see fig. 11)
ϵ_o	angle between emitted radiation and normal to flat surface, degrees (see fig. 11)
ζ	angle between azimuth of object slope and optical axis, degrees (see fig. 11)

η	scan efficiency
θ	angle between azimuth of incident and emitted radiation, degrees (see fig. 11)
θ_H	horizontal dimension of image frame, degrees
θ_V	vertical dimension of image frame, degrees
ι	angle between incident radiation and normal to sloped surface, degrees (see fig. 11)
ι_o	angle between incident radiation and normal to flat surface, degrees (see fig. 11)
λ	wavelength, meters
ξ	angle between optical axis and normal to δA_l, degrees (see fig. 10)
ρ_λ	spectral reflectivity of surface (normal albedo)
$\tau_\lambda(\iota_o)$	spectral transmissivity of atmosphere
$\tau_{\lambda,L}$	spectral transmissivity of optical path
Υ	optical thickness of Martian atmosphere
$\phi(\ )$	illumination scattering function
$\Delta\phi(\ )$	difference between values of the illumination scattering function for object and background
ψ	angle defining numerical aperture, degrees (see fig. 2)

Subscripts:

g	geometrical optics
p	physical optics

OPTICAL ANALYSIS

A basic configuration of an optical-mechanical scanner is shown in figure 1. The elements of concern to this analysis reduce simply to a lens and a pinhole. The lens is generally of small diameter and large focal ratio and can be made relatively free from aberrations. For this reason, only diffraction-limited lenses are considered. Because the detector is mounted flush on the pinhole or because the photons passing through the pinhole are guided by a field lens or light pipe to the detector, the diffraction produced by the pinhole has negligible effect.

The analysis is introduced in the spatial domain using first-order geometrical optics. It is then continued in the frequency domain because the techniques of Fourier transforms are more convenient to this analysis than the techniques of convolution used in the spatial domain for calculating the image distribution of a finite object. In both domains, the results from geometrical optics are extended to physical optics based on works of Wolf (ref. 9), Born and Wolf (ref. 10), and Hopkins (ref. 11). Since geometrical optics yield simpler but less accurate expressions than physical optics, results of these two methods are compared to assess the error introduced by using geometrical optics. Circular symmetry is assumed throughout; however, the results can be changed to accommodate rectangular configurations. Based on the results of this analysis, a tolerance for defect of focus is discussed.

Spatial-Domain Analysis

Definitions.- The optical geometry of lens and pinhole is shown in figure 2. The distance of the object from the lens L and the conjugate image distance l are related by the thin-lens formula:

$$\frac{1}{f} = \frac{1}{L} + \frac{1}{l} \tag{1}$$

where f is the lens focal length. The numerical aperture a_N is defined by

$$a_N = n \sin \psi = \frac{n \frac{D}{2}}{\left[\left(\frac{D}{2}\right)^2 + l^2\right]^{1/2}} \tag{2a}$$

where n is the index of refraction hereinafter considered equal to unity, and D is the lens diameter. Since generally $l \geqq f >> D$, the numerical aperture can be approximated by

$$a_N = \sin \psi = \frac{D}{2l} \tag{2b}$$

The instantaneous field of view, or angular scanning resolution, is described by the angle β as

$$\beta = 2 \tan^{-1} \frac{r_o}{l_o} \tag{3a}$$

where r_o is the radius of the pinhole or field stop, and l_o is the pinhole distance from the lens. For the small instantaneous fields of view associated with the optical-mechanical scanner, this relation reduces to

$$\beta = \frac{2r_o}{l_o} \tag{3b}$$

The radius R_o of a circular scan element in the object space is then approximately

$$R_o = \frac{1}{2} \beta L \tag{4a}$$

and the radius R of a circular object of any size is defined for later convenience by

$$R = bR_o = \frac{b}{2} \beta L \tag{4b}$$

where b is any real positive number.

Geometrical optics.- If the pinhole plane is in focus $(l = l_o)$, the area πR_o^2 has a well-defined meaning as a scan element since all the radiation emitted from this area and captured by the lens is also, according to first-order geometrical optics, incident on the pinhole. However, as soon as the pinhole plane is out of focus, the significance of πR_o^2 as a scan element becomes nebulous since the radiation emitted from this element area and captured by the lens is spread over an area larger than the pinhole and since some radiation emitted from the surrounding area is transmitted through the pinhole.

To gain a better understanding of the radiation distribution in the image space, an axial object point is considered. All the radiation emitted from this point and captured by the lens passes through the conjugate image point. (See fig. 3.) In a plane at a distance Δl from the conjugate image point, the image consists of a uniformly illuminated circular area of radius $\Delta r = \Delta l \tan \psi = \frac{D}{2l} \Delta l$.

It is useful at this stage to introduce the dimensionless variables u and v_o for the radii Δr and r_o, respectively. Similar notation is used by Wolf, Born and Wolf, and Hopkins (refs. 9, 10, and 11). Use of these variables allows the numerical results of the following equations to be readily used for a wide range of specific system configurations, the results being subject only to the restrictions under which the equations were derived.

$$u = \frac{2\pi}{\lambda} \sin \psi \, \Delta r = \frac{2\pi}{\lambda} \Delta l \tan \psi \sin \psi$$

$$v_o = \frac{2\pi}{\lambda} \sin \psi \, r_o$$

By substituting the approximation given by equation (2b) for $f >> D$, these expressions reduce to

$$u = \frac{2\pi}{\lambda}\left(\frac{D}{2l}\right)\Delta r = \frac{2\pi}{\lambda}\left(\frac{D}{2l}\right)^2 \Delta l \tag{5}$$

$$v_o = \frac{2\pi}{\lambda}\left(\frac{D}{2l}\right)r_o \tag{6}$$

The normalized fraction of the radiation captured by the lens from the axial object point which is transmitted through the pinhole may then be given by

$$\left.\begin{aligned} I_g(u,v_o) &= 1 & \qquad & \left(\frac{v_o}{u} \geqq 1\right) \\ I_g(u,v_o) &= \left(\frac{v_o}{u}\right)^2 & \qquad & \left(\frac{v_o}{u} \leqq 1\right) \end{aligned}\right\} \tag{7}$$

where the subscript g is used to indicate geometrical optics.

Physical optics.- A rigorous analysis of the light-intensity distribution at and near the focal plane of a diffraction-limited lens is presented in references 9 and 10. The following equations, obtained from these references and given in the notation of the present report, replace equation (7) for physical optics, provided that $f >> D >> \lambda$ and $f >> r_o$.

$$I_p(u,v_o) = 1 - \sum_{\mu=0}^{\infty} \frac{(-1)^{\mu}}{2\mu + 1}\left(\frac{u}{v_o}\right)^{2\mu} Q_{2\mu}(v_o) \tag{8a}$$

where

$$Q_{2\mu}(v_o) = \sum_{\nu=0}^{2\mu} (-1)^{\nu}\left[J_{\nu}(v_o)J_{2\mu-\nu}(v_o) + J_{\nu+1}(v_o)J_{2\mu+1-\nu}(v_o)\right] \tag{8b}$$

The variables u and v_o are given by equations (5) and (6), respectively, and J_n is the nth order Bessel function. The subscript p is used to indicate physical optics. For ease of computation, the expression for the dummy variable $Q_{2\mu}(v_o)$ may also be written as

$$Q_{2\mu}(v_o) = 2\sum_{\nu=0}^{\mu-1}(-1)^{\nu}\left[J_{\nu}(v_o)J_{2\mu-\nu}(v_o) + J_{\nu+1}(v_o)J_{2\mu+1-\nu}(v_o)\right] + (-1)^{\mu}\left[J_{\mu}^{2}(v_o) + J_{\mu+1}^{2}(v_o)\right] \tag{8c}$$

When $\frac{v_o}{u} < 1$, the series given by equation (8a) converges slowly and the following relations are preferable:

$$I_p(u,v_o) = \left(\frac{v_o}{u}\right)\left[1 + \sum_{\mu=0}^{\infty} \frac{(-1)^{\mu}}{2\mu + 1}\left(\frac{v_o}{u}\right)^{2\mu} Q_{2\mu}(v_o)\right]$$

$$- \frac{4}{u}\left[Y_1(u,v_o)\cos \frac{1}{2}\left(u + \frac{{v_o}^2}{u}\right) + Y_2(u,v_o)\sin \frac{1}{2}\left(u + \frac{{v_o}^2}{u}\right)\right] \tag{8d}$$

where the variable $Q_{2\mu}(v_o)$ is again given by equation (8c), and Y_1 and Y_2 are two of the functions of

$$Y_j(u,v_o) = \sum_{\mu=0}^{\infty} (-1)^{\mu}(j + 2\mu)\left(\frac{v_o}{u}\right)^{j+2\mu} J_{j+2\mu}(v_o) \tag{8e}$$

If $\frac{u}{v_o} = 1$, equation (8a) reduces to

$$I_p(u,u) = 1 - J_0(u)\cos u - J_1(u)\sin u \tag{8f}$$

And if the pinhole detector is in geometrical focus ($\Delta l = 0$), this equation reduces to

$$I_p(0,v_o) = 1 - {J_0}^2(v_o) - {J_1}^2(v_o) \tag{8g}$$

Numerical results of these equations are presented later. While the results for the spatial image distribution of a point source can be extended to sources of finite area by using the techniques of convolution, the techniques of Fourier transforms are generally more convenient and will now be discussed.

Frequency-Domain Analysis

Definitions.- Spatial distribution $F(x,y)$ and frequency distribution $f(k_x,k_y)$ are related by the Fourier transform pair (ref. 12)

$$f(k_x,k_y) = \int_{-\infty}^{\infty}\int_{-\infty}^{\infty} F(x,y)e^{-i2\pi(k_x x+k_y y)}dx\,dy \tag{9a}$$

$$F(x,y) = \int_{-\infty}^{\infty}\int_{-\infty}^{\infty} f(k_x,k_y)e^{i2\pi(k_x x+k_y y)}dk_x\,dk_y \tag{9b}$$

For circular symmetry about the optical axis, these relations reduce to the Hankel transforms (ref. 12)

$$f(k) = 2\pi \int_0^\infty F(r)J_0(2\pi rk)r\,dr \qquad (10a)$$

$$F(r) = 2\pi \int_0^\infty f(k)J_0(2\pi rk)k\,dk \qquad (10b)$$

where $r = \left(x^2 + y^2\right)^{1/2}$ and $k = \left(k_x^2 + k_y^2\right)^{1/2}$.

Again, to generalize the following formulas, it is convenient to introduce the dimensionless variable s for the spatial frequency k in lines per unit length of wavelength by

$$s = \frac{\lambda}{\sin \psi} k \qquad (11a)$$

or for $f >> D$ by

$$s = \lambda\left(\frac{2l}{D}\right)k \qquad (11b)$$

Geometrical optics.- The Fourier transform of the spatial intensity distribution of a point source image is the modulation transfer function (MTF) of the imaging lens. The out-of-focus image of a point source is a circular area of constant intensity with a radius Δr as illustrated in figure 3. By using the dimensionless variable u (eq. (5)) for Δr and the dimensionless variable $v = \frac{2\pi}{\lambda}(\sin \psi)r = \frac{2\pi}{\lambda}\left(\frac{D}{2l}\right)r$ for r and by using the Hankel transform given by equation (10a), the defocused lens MTF becomes

$$d_g(u;s) = \frac{2\pi \int_0^u J_0(vs)v\,dv}{\int_0^{2\pi} \int_0^u v\,dv\,d\omega} = \frac{2J_1(us)}{us} \qquad (12)$$

when normalized to make $d_g(u;0) = 1$.

Similarly, the frequency response (MTF) of the pinhole with radius v_o is

$$p(v_o;s) = \frac{2\pi \int_0^{v_o} J_0(vs)v\,dv}{\int_0^{2\pi} \int_0^{v_o} v\,dv\,d\omega} = \frac{2J_1(v_o s)}{v_o s} \qquad (13)$$

when normalized to make $p(v_o;0) = 1$. The optical system MTF is then given by the product of the lens and pinhole MTF $d_g(u;s)p(v_o;s)$.

Physical optics.- A complete analysis of the frequency response of a diffraction-limited lens with an out-of-focus image plane is presented in reference 11. The following equations, obtained from this reference and given in the notation of the present report, replace equation (12) for physical optics:

$$d_p(u;s) = \frac{4}{\pi us}\cos\left(\frac{1}{2}us^2\right)\left\{\gamma J_1(us) + \frac{1}{2}\sin 2\gamma\left[J_1(us) - J_3(us)\right]\right.$$

$$\left. - \frac{1}{4}\sin 4\gamma\left[J_3(us) - J_5(us)\right] + \dots\right\}$$

$$- \frac{4}{\pi us}\sin\left(\frac{1}{2}us^2\right)\left\{\sin\gamma\left[J_0(us) - J_2(us)\right]\right.$$

$$\left. - \frac{1}{3}\sin 3\gamma\left[J_2(us) - J_4(us)\right] + \frac{1}{5}\sin 5\gamma\left[J_4(us) - J_6(us)\right] - \dots\right\} \tag{14a}$$

The variables u and s are given by equations (5) and (11), respectively, and $\gamma = \cos^{-1}\left(\frac{s}{2}\right)$. As the pinhole plane approaches focus ($\Delta l = 0$), this response function becomes

$$d_p(0;s) = \frac{1}{\pi}(2\gamma - \sin 2\gamma) \tag{14b}$$

The optical system MTF becomes then according to physical optics the product $d_p(u;s)p(v_o;s)$. As explained before, diffraction produced by the pinhole has no effect. Numerical results of these equations are presented later.

Image of Circular Object

A circular area with a radius defined by equation (4b) is a convenient target for evaluating the optical system response. In particular, the circular object becomes the scan element for the constant b equal to unity, and the resolution element for b equal to the Kell factor $\sqrt{2}$ (ref. 13). The brightness of the circular object area is considered to be unity in this section; the actual brightness value is derived in the section containing the radiometric analysis.

To continue the analysis with dimensionless variables, the radius of the in-focus image of the circular object is, according to geometrical optics, defined by bv_o. The image frequency spectrum for an out-of-focus pinhole plane is the product $\frac{2J_1(bv_os)}{bv_os}\frac{2J_1(v_os)}{v_os}d(u;s)$, according to geometrical optics for $d_g(u;s)$ and physical optics for $d_p(u;s)$. Since the inverse Fourier transform of the image frequency distribution yields the image spatial distribution $P(u,v_o;b,v)$, the latter becomes

$$P(u,v_0;b,v) = \frac{b^2 v_0^2}{2} \int_0^\infty \frac{2J_1(bv_0 s)}{bv_0 s} \frac{2J_1(v_0 s)}{v_0 s} d(u;s) J_0(vs) s \, ds \tag{15}$$

The value $b^2 v_0^2/2$ is a normalization factor which assures that the peak image level $P(u,v_0;b)$ occurring at $v = 0$ and given by

$$P(u,v_0;b) = \frac{b^2 v_0^2}{2} \int_0^\infty \frac{2J_1(bv_0 s)}{bv_0 s} \frac{2J_1(v_0 s)}{v_0 s} d(u;s) s \, ds \tag{16}$$

is equal to unity for a perfect optical system $(d(0;s) = 1)$ if $b \geqq 1$.* If $b < 1$, $P(u,v_0;b)$ should be less than unity even for a perfect optical system because then the in-focus geometrical image of the standard target is smaller than the pinhole area but is integrated over this area by the detector.

Evaluation and Comparison of Geometrical and Physical Optics

The normalized fraction of the radiation captured by a lens from an axial object point which is transmitted through the pinhole, as given by equation (7) for geometrical optics and by equation (8) for physical optics, is plotted in figure 4. The frequency response (MTF) of a defocused lens, as given by equations (12) and (14) for geometrical and physical optics, respectively, is plotted in figure 5. Several tables of this frequency-response function have been published in reference 15. Because of the similarity between equations (12) and (13), the pinhole MTF may be obtained from figure 5(a) simply by replacing u with v_0 and $d_g(u;s)$ with $p(v_0;s)$.

Similar results have also been presented and discussed elsewhere (refs. 9, 10, and 11) and have led to general conclusions which may briefly be summarized as follows: Errors in geometrical optics decrease as (1) the pinhole area and lens aperture increase, (2) the defects of focus increase, and (3) the spatial-frequency components of the target decrease.

---

*It can be shown (see, for example, ref. 14) that

$$\frac{b^2 v_0^2}{2} \int_0^\infty \frac{2J_1(bv_0 s)}{bv_0 s} \frac{2J_1(v_0 s)}{v_0 s} s \, ds = 1$$

if $b \geqq 1$, and that

$$\frac{v_0^2}{2} \int_0^\infty \frac{2J_1(bv_0 s)}{bv_0 s} \frac{2J_1(v_0 s)}{v_0 s} s \, ds = 1$$

if $b < 1$.

The effects of out-of-focus blur on the performance of an optical-mechanical scanner which are most directly pertinent to this analysis can best be observed from figures 6 and 7. In figure 6, the normalized image distribution $P_p(u,v_o;b=1,v)$ of a scan element is plotted as a function of the dimensionless radial distance v from the optical axis, according to physical optics. In figure 7, the distribution $P_g(u,v_o;b=1,v)$ is plotted according to geometrical optics. In both figures, curves are plotted for various amounts of defocus represented by the dimensionless variable u (eq. (5)) as a function of the dimensionless pinhole radius v_o (eq. (6)).

For geometrical optics, figure 7 provides a convenient means for predicting the effect of various amounts of defocus on the image of a scan element for any value of v_o. However, for physical optics the value of v_o is important for determining the image distribution. Plots for different values of v_o are, therefore, presented in figure 6.

As can be observed by comparing figures 6 and 7, the accuracy of geometrical optics increases as u and v_o increase and, conversely, decreases as u and v_o decrease.

Tolerance for Defect of Focus

Since some resolution degradation due to defect of focus is inevitable, a criterion must be established for the amount of blur which is to be tolerated. Although such a criterion cannot escape from being somewhat arbitrary in the absence of a specific goal, the severely limited transmission capacity of small planetary landers suggests that the maximum out-of-focus image resolution should not be allowed to degrade significantly below the sampling resolution of the scanning aperture; otherwise, a lower sampling resolution may be more advantageous. A criterion which satisfies such a requirement and which is also simple to calculate and easy to interpret in terms of the preceding results is given by the familiar depth of field of a camera. The depth of field ΔL is generally given in a form similar to that given in reference 16

$$\frac{DL_of}{2r_oL_o - 2r_of - Df} \leqq \Delta L \leqq \frac{DL_of}{Df - 2r_oL_o + 2r_of} \tag{17a}$$

where L_o is the object distance in geometrical focus. Upon substituting $\frac{1}{l_o} = \frac{1}{L_o} - \frac{1}{f}$ and $\beta = \frac{2r_o}{l_o}$, equation (17a) may also be written as

$$\frac{D/\beta}{\frac{D}{\beta L_o} + 1} \leqq \Delta L \leqq \frac{D/\beta}{\frac{D}{\beta L_o} - 1} \tag{17b}$$

The depth of field is conventionally derived from geometrical tracings in which the pinhole is interpreted as the circle of confusion. (See fig. 3.) As is apparent from this figure, the depth of field is the distance which can be traversed by an object point source and still allow, according to geometrical optics, all the radiant energy captured by the lens to be incident on the pinhole. At the limits of depth of field, the radius Δr equals r_o. The effects of the resulting degradation on the image of a scan element which is tolerated by this criteria can, therefore, be readily observed from figures 6 and 7 for $u = v_o$. The variation of the degraded peak image level $P_p\left(v_o,u=v_o;b\right)$ with v_o is plotted in figure 8, both for the scan element $(b = 1)$ previously considered and a resolution element $\left(b = \sqrt{2}\right)$.

RADIOMETRIC ANALYSIS

As the optical-mechanical scanner surveys the surrounding terrain (fig. 9), its viewing geometry varies continuously with respect to the incident radiation. Hence, the apparent surface radiance and object contrast and, therefore, the image quality vary also. If all the information that is implicit in the image, regardless of the possible complexity of the interpretation, must be extracted, the quality of the image is most appropriately assessed by its signal-to-noise ratio. (See ref. 17.) Accordingly, a signal-to-noise ratio is derived to predict image quality.

The analysis is introduced with the derivation of an expression for the spectral radiant power emitted from the surface and captured by the instantaneous field of view of the optical system, with only in-focus geometric optics considered. The apparent variation of this radiant power with viewing geometry is then investigated and the resulting detector signal-to-noise-ratio output is presented. Only the noise generated by the radiation detectors is considered, and all further degradation of the signal before final reconstruction is disregarded. Finally, the effects of aperture diffraction and out-of-focus blur on the signal-to-noise ratio of the image of the circular object, as discussed in the foregoing analysis, are included.

Spectral Radiant Power

The equation for the spectral radiant power P_λ emitted by an elemental area δA_o and incident upon another elemental area δA_l (fig. 10) may be obtained from reference 18

$$P_\lambda = N_\lambda \frac{\left(\delta A_o \cos \epsilon\right)\left(\delta A_l \cos \xi\right)}{L^2} \tag{18}$$

The spectral radiance N_λ of the surface may generally be given by the following equation obtained from reference 19

$$N_\lambda = \frac{1}{\pi} S_\lambda \tau_\lambda(\iota_o)\rho_\lambda \phi(\epsilon, \iota, g) \tag{19}$$

where S_λ is the solar irradiance, $\tau_\lambda(\iota_o)$ the transmissivity of the atmosphere, ρ_λ the reflectivity (normal albedo), and $\phi(\epsilon,\iota,g)$ the illumination scattering function of the surface. If ρ_λ is defined as bond albedo, then the factor $\frac{1}{\pi}$ should be replaced by $\frac{2}{3\pi}$ (ref. 19). In equation 18, the elemental surface area $\delta A_o \cos \epsilon$, projected normal to the optical axis, may be replaced by the scan-element area πR_o^2 of uniform luminance since $L >> R_o$. And since the lens aperture is normal to the optical axis, that is, $\xi = 0$, the elemental area δA_l may be replaced by the lens-aperture area $\frac{\pi}{4} D^2$.

Upon proper substitution and the inclusion of a loss factor $\tau_{\lambda,L}$ due to the transmissivity of the optical path, the spectral radiant power incident upon the pinhole becomes

$$P_\lambda = \frac{\pi}{4} \frac{R_o^2 D^2 S_\lambda \tau_\lambda(\iota_o)\rho_\lambda \tau_{\lambda,L}\phi(\epsilon,\iota,g)}{L^2} \tag{20a}$$

or in terms of the instantaneous field of view (eq. (4a))

$$P_\lambda = \frac{\pi}{16} \beta^2 D^2 S_\lambda \tau_\lambda(\iota_o)\rho_\lambda \tau_{\lambda,L}\phi(\epsilon,\iota,g) \tag{20b}$$

Viewing Geometry

The illumination scattering function $\phi(\epsilon,\iota,g)$ accounts for the dependence of surface reflectance on viewing geometry as illustrated in figure 11. This function depends on the angle ι between incident radiation and surface normal, the angle ϵ between emitted radiation and surface normal, and the phase angle g between incident and emitted radiation. To determine $\phi(\epsilon,\iota,g)$, the angles ϵ, ι, and g must be expressed as functions of the optical-mechanical-scanner viewing geometry and the target slope. The magnitude of the surface slope of the circular object is defined by the angle α and its azimuth with respect to the optical axis of the optical-mechanical scanner is defined by ζ. The unit vector normal to a surface of slope α is defined by $\hat{N}$ and that normal to a surface of zero slope is defined by $\hat{N}_o$. Finally, the angle between the incident radiation and $\hat{N}_o$ is given by ι_o and that between the emitted radiation and $\hat{N}_o$ by ϵ_o. The angular relationships are derived by using spherical coordinate transformations as

$$\cos g = \cos \epsilon_o \cos \iota_o - \sin \epsilon_o \sin \iota_o \cos \theta \tag{21}$$

$$\cos \iota = \cos \alpha \cos \iota_o - \sin \alpha \sin \iota_o \cos(\theta - \zeta) \tag{22}$$

$$\cos \epsilon = \cos \alpha \cos \epsilon_o - \sin \alpha \sin \epsilon_o \cos(180^\circ - \zeta) \tag{23}$$

For the purpose of this analysis, the object and background are considered to be of the same material and to differ only in slope. The radiance difference between target and background is then dependent only on the illumination scattering function as given by

$$\Delta\phi(\epsilon,\iota,g;\alpha,\zeta) = \phi(\epsilon,\iota,g;\alpha,\zeta) - \phi(\epsilon_o,\iota_o,g) \tag{24}$$

where $\phi(\epsilon_o,\iota_o,g)$ is the value of the illumination scattering function for a flat background and $\phi(\epsilon,\iota,g;\alpha,\zeta)$ for the sloped object surface. The value $\Delta\phi(\epsilon,\iota,g;\alpha,\zeta)$ is positive if the target is brighter than the background and negative if darker.

Signal-to-Noise Ratio

Only objects near the system resolution limit which yield images of low contrast or objects which have low contrast are of general concern here. The signals to be detected are, therefore, small changes of radiation in a much larger and comparatively constant background radiation level. Accordingly, a spectral-radiance difference ΔN_λ between the target and background may be defined as

$$\Delta N_\lambda = \frac{1}{\pi} S_\lambda \tau_\lambda(\iota_o)\rho_\lambda \, \Delta\phi(\epsilon,\iota,g;\alpha,\zeta) \tag{25}$$

and, similarly, a spectral-radiant-power difference ΔP_λ may be defined as

$$\Delta P_\lambda = \frac{\pi}{16} \beta^2 D^2 S_\lambda \tau_\lambda(\iota_o)\rho_\lambda \tau_{\lambda,L} \, \Delta\phi(\epsilon,\iota,g;\alpha,\zeta) \tag{26}$$

by replacing $\phi(\epsilon,\iota,g)$ with $\Delta\phi(\epsilon,\iota,g;\alpha,\zeta)$ in equations (19) and (20), respectively.

A standard expression for the noise-equivalent power of a solid-state detector from reference 20 in the notation of the present report is

$$(\mathrm{NEP})_\lambda = \frac{(A_D W)^{1/2}}{D^*_\lambda} \tag{27}$$

where A_D is the detector area and W the video bandwidth. The signal-to-rms-noise ratio at the output of the detector is the ratio of the spectral-radiant-power difference ΔP_λ sensed by the detector over the noise-equivalent-power $(\mathrm{NEP})_\lambda$ integrated over the wavelength-sensitive range of the detector.

$$\frac{S}{N} = \int_{\lambda_1}^{\lambda_2} \frac{\Delta P_\lambda}{(\mathrm{NEP})_\lambda} \, d\lambda = \frac{\pi\beta^2 D^2 \, \Delta\phi(\epsilon,\iota,g;\alpha,\zeta)}{16(A_D W)^{1/2}} \int_{\lambda_1}^{\lambda_2} S_\lambda \tau_\lambda(\iota_o)\rho_\lambda \tau_{\lambda,L} D^*_\lambda \, d\lambda \tag{28}$$

where β is given in radians.

A related figure of merit is the noise-equivalent-radiance difference ΔNER. An expression for the ΔNER can be obtained by using the relation from reference 20

$$\Delta NER = \frac{N}{S}\int_{\lambda_1}^{\lambda_2} \Delta N_\lambda \, d\lambda \tag{29}$$

Upon substitution of equation (28) for S/N and equation (25) for the spectral radiance difference in equation (29), the ΔNER becomes

$$\Delta NER = \left(\frac{4}{\pi}\right)^2 \frac{(A_D W)^{1/2}}{\beta^2 D^2} \frac{\int_{\lambda_1}^{\lambda_2} S_\lambda \tau_\lambda(\iota_o)\rho_\lambda \, d\lambda}{\int_{\lambda_1}^{\lambda_2} S_\lambda \tau_\lambda(\iota_o)\rho_\lambda \tau_{\lambda,L} D_\lambda^* \, d\lambda} \tag{30}$$

These results do not account for the image degradation of targets near the angular resolution of the system by out-of-focus blur and diffraction. This degradation was evaluated in the preceding optical analysis and described by the normalized peak image signal level $P(u,v_o;b)$ in equation (15). Since $P(u,v_o;b)$ is wavelength dependent according to physical optics, it must be included in the wavelength integral as shown:

$$\left(\frac{S}{N}\right)_P = \frac{\pi\beta^2 D^2 \Delta\phi(\epsilon,\iota,g;\alpha,\zeta)}{16(A_D W)^{1/2}} \int_{\lambda_1}^{\lambda_2} S_\lambda \tau_\lambda(\iota_o)\rho_\lambda \tau_{\lambda,L} D_\lambda^* P_p(u,v_o;b)d\lambda \tag{31}$$

The function $P(u,v_o;b)$ may be moved outside the integral if geometrical optics are considered.

Video Bandwidth

As revealed by equation (28), the image signal-to-noise ratio is inversely proportional to the square root of the video bandwidth. Adjusting the acquisition rate of the optical-mechanical scanner to the video-transmission rate to allow buffer-free operation would, therefore, relate the signal-to-noise ratio to the transmission rate.

If the optical-mechanical scanner surveys the surrounding scene with a scanning resolution β in degrees over a horizontal and vertical field of view θ_H and θ_V, respectively, the number of independent samples or scan elements contained in the resulting frame is $\theta_H\theta_V/\beta^2$. If, furthermore, the frame is acquired during a time interval t_f and the scanning efficiency is η, the sampling or dwell time for each scan element is

$$t_d = \frac{\beta^2 \eta t_f}{\theta_V \theta_H} \tag{32}$$

By assuming a Nyquist sampling rate, an equation for the video bandwidth in the notation of the present report can be obtained from reference 21.

$$W = \frac{1}{2t_d} = \frac{\theta_H \theta_V}{2\beta^2 \eta t_f} \tag{33}$$

If this bandwidth-limited analog signal is encoded to 2^m binary levels, then the corresponding transmission rate is

$$T = 2mW = \frac{m\theta_H \theta_V}{\beta^2 \eta t_f} \tag{34}$$

TRADE-OFF ANALYSIS FOR THE MARTIAN ENVIRONMENT

Results of the foregoing analysis are now used to evaluate the performance of the optical-mechanical scanner in a Martian environment. Emphasis is placed on the trade-off between signal-to-noise ratio, angular scanning resolution, tolerance for defect of focus, and video-acquisition rate. The evaluation is introduced by calculating the variation of signal-to-noise ratio and acquisition rate with angular scanning resolution and lens aperture for various brightness differences between target and background, with only in-focus geometrical optics considered. By selecting combinations of various scanning resolutions and lens apertures which yield equal signal-to-noise ratios for a given acquisition rate, their tolerance for defect of focus is then investigated. Finally, based on a trade-off between these parameters, a system is selected to illustrate the variation of the image signal-to-noise ratio of a scan element with a specified slope as the optical-mechanical scanner surveys the surrounding terrain. Pertinent properties of a model of the Martian environment currently used for the preliminary Viking lander design and mission planning are also used in this analysis and are given in appendix A. Pertinent characteristics of components of the optical-mechanical scanner are listed in appendix B to allow a practical application of the analysis, but not to suggest any optimum components.

Signal-to-Noise Ratio and Video Bandwidth

To evaluate the variation of the product of signal-to-noise ratio and video bandwidth with the product of lens diameter and angular scanning resolution, the signal-to-rms-noise ratio for a solid-state detector (eq. (28)) is rewritten in the form

$$\frac{S}{N}\sqrt{W} = \beta^2 D^2 \Delta\phi(\epsilon,\iota,g;\alpha,\zeta)\left[\frac{\pi}{16(57.3)^2\sqrt{A_D}}\int_{\lambda_1}^{\lambda_2} S_\lambda \tau_\lambda(\iota_o)\rho_\lambda \tau_{\lambda,L} D_\lambda^* \, d\lambda\right]$$

where the angular scanning resolution β is now given in degrees and the lens diameter is in centimeters. For the properties of the Martian environment and optical-mechanical scanner components given in appendixes A and B, respectively, the bracketed expression becomes $4.3 \times 10^7 \sqrt{Hz}/(\text{deg-cm})^2$. By using this value, the variation of $\frac{S}{N}\sqrt{W}$ with βD is plotted in figure 12.

Angular Scanning Resolution and Tolerance for Defect of Focus

For a trade-off between angular scanning resolution and tolerance for defect of focus, the optical-mechanical scanner is grouped for convenience into low- and high-resolution systems. The low-resolution system may typically be employed to survey the entire surrounding terrain, and the high-resolution system to take close looks at areas of special interest. The low-resolution system must, therefore, be capable of scanning from close to the lander to the horizon, which would mean covering object distances from about 1 or 2 meters to infinity within a single frame. The high-resolution system, on the other hand, needs to be capable of scanning only a fraction of this range of object distances within one frame and may be refocused between frames. Thus, the low-resolution system is required to have a larger tolerance to out-of-focus blur than the high-resolution system. The dividing line between these two resolutions is arbitrarily drawn by the normal capability of the human eye which has an angular resolution of 0.05° under favorable lighting conditions for objects displaying a contrast of 0.2 (ref. 22), contrast being defined as the ratio of the luminance difference between the bright and dark areas of the test object divided by the luminance sum. By considering various combinations of angular scanning resolution and lens diameter which yield equal signal-to-noise ratios according to figure 12, the corresponding tolerance for defect of focus is plotted versus the in-focus distance in figure 13. As discussed in the optical analysis, the conventional depth of field given by equation (17) is used as a criterion for the acceptable degradation from out-of-focus blur. Depth of field may be read from these curves as illustrated in figure 13(b) for $\beta D = 0.004$ deg-cm. For an angular scanning resolution $\beta = 0.01^\circ$ and for an in-focus distance $L_o = 15$ meters, the corresponding depth of field ΔL ranges from 9 to 48 meters.

Illustration of Trade-Off and Performance

Taken together, figures 12 and 13 provide the means for a preliminary trade-off between signal-to-noise ratio, angular scanning resolution, tolerance for defect of focus, and video acquisition rate, as will be illustrated first for low-scanning resolutions and then for high-scanning resolutions.

Low-resolution survey.- It is assumed that the entire scene surrounding a planetary lander must be surveyed under the constraints that the angular resolution be 0.1°, that the video acquisition rate be matched to a transmission rate of $T = 20\ 000$ bits/sec, and that acceptable depth of field be achieved without focus control. According to the relation

$T = 2mW$, the corresponding video bandwidth is about $W = 1600$ hertz for a 64-level encoding ($m = 6$). From figure 13(a), an acceptable tolerance for defect of focus extending over a range from less than 1.0 meter to infinity can be observed for $\beta D = 0.03$ deg-cm and $L_o = 2$ meters. The required lens diameter would be 0.3 cm. Values of the product $\frac{S}{N}\sqrt{W}$ resulting from the product $\beta D = 0.03$ deg-cm for various values of $\Delta\phi$ can be observed from figure 12. For a solid-state detector, a signal-to-noise ratio of nearly 9 is obtained for $\Delta\phi = 0.01$. The variation of the peak signal-to-rms-noise ratio of a scan element (eq. (31), $b = 1$) with a slope of 6° and a slope azimuth with respect to the optical axis of 0° is plotted in figure 14. Incident solar angles of 30° and 60° are considered. The scanner height is assumed to be 1.5 meters. Scanner height determines the object distance for any angular geometry and, therefore, the amount of out-of-focus blur. Similarly, the average background signal level obtained by replacing $\Delta\phi(\epsilon,\iota,g;\alpha,\zeta)$ by $\phi(\epsilon_o,\iota_o,g)$ in equation (28) is plotted in figure 15.

Important to observe in figure 14 is the variation of signal-to-noise ratio and, therefore, detectivity of fine detail which is the primary objective of the imaging experiment. Positive values of the signal-to-noise ratios indicate images of the slope which are brighter than the background and negative values indicate images which are darker. Also important to observe in figure 15 is the wide variation in background signal level not only in each frame but also in each line scan. These variations of brightness and contrast depend, of course, on the illumination scattering function of the surface. The function used here was derived by Hapke (see appendix A) for the lunar surface. Little corresponding data are available for the Martian surface. These and similar results can serve, therefore, only approximately for a viewing strategy. However, these results do clearly reveal the need for an automatic gain control to encode the video signal efficiently.

High-resolution imagery.- As revealed by the data plotted in figure 13(b), high-resolution optical-mechanical scanners have only limited depth of field, even at substantially reduced values of βD, and, therefore, require some form of focus control. Focus controls may roughly be classified into three groups: discrete, continuous, and automatic. Discrete focus controls provide a single focus setting for each image frame of a limited field of view. Continuous focus controls provide a continuous change of distance between lens and pinhole. For some image-space line scanners, this motion can be incorporated into the line-scan mechanism; for an object-space line scanner, this motion requires an additional moving mechanism which is geared to the line-scan drive. For either line scanner, this focus mechanism would be designed to maintain focus to a flat, featureless surface. A sufficient depth of field is then still needed to accommodate any deviations from this surface, such as rocks and craters. The discrete and continuous focus control can, of course, be combined for increased versatility and reliability. Automatic focus controls also provide a continuous change of distance between lens and pinhole, but this motion is controlled by a servomechanism which relies on the video signal itself for focusing. The reduction of high-frequency components in the video signal associated with out-of-focus blur could be sensed and used to drive the focus mechanism.

The selection of a high-resolution optical-mechanical scanner thus depends not only on a trade-off between the factors analyzed herein, but also on the acceptable level of complexity of the focus-control mechanism. And as illustrated, highly accurate focus controls are required for angular resolutions approaching 0.01°.

CONCLUDING REMARKS

An analytical study was presented of the effects of a continuously varying object distance and viewing geometry on the performance of an optical-mechanical scanner as it surveys the terrain surrounding a planetary lander. The study was divided into an optical analysis of the image quality degradation due to varying out-of-focus blur during each line scan, a radiometric analysis of the varying image signal-to-noise ratio of small targets during each frame, and an application of the results of these analyses to illustrate trade-offs between major performance parameters. These parameters were signal-to-noise ratio, angular scanning resolution, tolerance for defect of focus, and video-acquisition rate. They were found to be so closely interrelated that any improvement in one or more could only be accomplished at the expense of the others.

Evaluation of the in- and out-of-focus image distribution of targets near the resolution threshold of the optical-mechanical scanner was performed according to geometrical and physical optics. Comparison of the relatively simple results of the geometrical and physical optics revealed that geometrical optics yield estimates of increasing accuracy as the scanning resolution is widened and the out-of-focus blur is increased. Conversely, however, as the scanning resolution is narrowed and the out-of-focus blur is diminished to tolerable amounts, errors introduced by geometrical optics become significant. A general criterion for the tolerance for defect of focus is perhaps best governed by the consideration that the resolution of the out-of-focus image should not be significantly lower than the sampling resolution; otherwise, the information capacity of the video-transmission link would be poorly utilized. As was illustrated, the conventional definition of the depth of field of a camera yields a simple and acceptable criterion.

A preliminary trade-off between the performance parameters analyzed herein was demonstrated for a model of the Martian environment currently used for the Viking lander design and mission planning. The optical-mechanical scanner was divided for this purpose into low- and high-resolution systems, with the former defined as being wider than the 0.05° angular resolution of the normal unaided human eye and the latter as being narrower. With the video-acquisition rate matched to a transmission rate of 20 000 bits/sec, low-resolution systems were found to be capable of surveying the entire surrounding terrain with sufficient signal-to-noise ratios to detect low slopes of targets near their angular scanning resolution without requiring focus control. High-resolution systems, however, were found to require focus controls of increasing accuracy and, therefore, complexity as angular resolutions of 0.01° are approached. A wide variation in the average background signal level was found not only in each frame but also in each line scan, requiring an automatic gain control to encode the video signal efficiently.

Langley Research Center,
National Aeronautics and Space Administration,
Langley Station, Hampton, Va., September 30, 1969.

APPENDIX A

MARTIAN ENGINEERING MODEL

This appendix contains properties of a Martian engineering model which are pertinent to this analysis and which have been used in the preliminary design of the Viking lander. These properties are solar radiation, transmissivity of the atmosphere, spectral reflectivity of the surface, and illumination scattering function of the surface.

Solar Radiation

The variation of solar radiation at 1.0 astronomical unit $S_{\lambda,u}$ with wavelength is plotted in figure 16. The distance of Mars from the sun varies from a minimum of 1.52 to a maximum of 1.67 AU during 1974; for convenience, 1.6 AU is used for this study. The solar radiation above the Martian atmosphere is, therefore, given by $S_\lambda = S_{\lambda,u}/(1.6)^2$.

Transmissivity of Atmosphere

The transmissivity of the Martian atmosphere is given by the expression

$$\tau_\lambda(\iota_o) = e^{-\Upsilon/\cos \iota_o} \tag{A1}$$

where Υ is the optical thickness plotted in figure 17 and ι_o the incident angle of the solar radiation.

Spectral Reflectivity

The spectral reflectivity of the Martian surface ρ_λ is plotted in figure 18 for areas of intermediate brightness. It is considered higher for bright areas by a factor of 1.33 and lower for dark areas by a factor of 0.66.

Illumination Scattering Function

The illumination scattering function is the improved photometric function of the lunar surface derived by Hapke (ref. 23) and given by the expression

$$\phi(\epsilon,\iota,g) = C_1(\sigma,g)C_2(g)C_3(g) \tag{A2}$$

where

$$C_1(\sigma,g) = \frac{K_1\left(1 - c_1\right)}{1 + \dfrac{\cos \sigma}{\cos(\sigma + g)}} + \frac{K_2 c_1}{2 \cos \frac{g}{2} \cos \sigma \sin \gamma}\left[\cos\left(\sigma + K_3 g\right)\sin\left(\gamma + K_4 g\right)\right.$$

$$\left. - \frac{1}{2} \sin^2 \frac{g}{2} \ln\left|\frac{\cos\left(\sigma + K_3 g\right) + \sin\left(\gamma + K_4 g\right)}{\cos\left(\sigma + K_3 g\right) - \sin\left(\gamma + K_4 g\right)}\right|\right]$$

$$C_2(g) = \frac{1}{\pi}\left[\sin|g| + \left(\pi - |g|\cos|g|\right)\right] + 0.1\left(1 - \cos|g|\right)^2$$

$$C_3(g) = 2 - \frac{\tan|g|}{2c_2}\left(1 - e^{-c_2/\tan|g|}\right)\left(3 - e^{-c_2/\tan|g|}\right) \qquad \left(|g| \leqq \frac{\pi}{2}\right)$$

$$C_3(g) = 1 \qquad \left(|g| \geqq \frac{\pi}{2}\right)$$

The parameter σ is the luminance longitude and is related to the incidence angle ι, emission angle ϵ, and phase angle g by

$$\sigma = \tan^{-1}\left(\frac{\cos \epsilon \cos g - \cos \iota}{\cos \epsilon \sin g}\right) \tag{A3}$$

The constants K_1, K_2, K_3, and K_4 have different values depending on σ and g, as given in the following table. Only values appropriate to $g \geqq 0$ are given; the photometric function is symmetric with respect to a simultaneous change of sign of σ and g. The other constants are $c_1 = 0.9$, $c_2 = 0.4$, and $\gamma = 45^o$.

Region		K_1	K_2	K_3	K_4
for σ –	for g –				
$-\frac{\pi}{2} \leqq \sigma \leqq \frac{\pi}{2}$	$\left(\frac{\pi}{2} - \sigma\right) \leqq g \leqq \pi$	0	0		
$\left(-\frac{\pi}{2} + \gamma\right) \leqq \sigma \leqq \frac{\pi}{2}$	$\left(\frac{\pi}{2} - \gamma - \sigma\right) \leqq g \leqq \left(\frac{\pi}{2} - \sigma\right)$	1	1	1	$\frac{1}{2}$
$\left(-\frac{\pi}{2} + \gamma\right) \leqq \sigma \leqq \left(\frac{\pi}{2} - \gamma\right)$	$0 \leqq g \leqq \left(\frac{\pi}{2} - \gamma - \sigma\right)$	1	1	$\frac{1}{2}$	0
$-\frac{\pi}{2} \leqq \sigma \leqq \left(-\frac{\pi}{2} + \gamma\right)$	$0 \leqq g \leqq \left(\frac{\pi}{2} - \gamma - \sigma\right)$	1	1	0	$\frac{1}{2}$
$-\frac{\pi}{2} \leqq \sigma \leqq \left(-\frac{\pi}{2} + \gamma\right)$	$\left(\frac{\pi}{2} - \gamma - \sigma\right) \leqq g \leqq (\pi - \sigma)$	1	1	$\frac{1}{2}$	1
$-\frac{\pi}{2} \leqq \sigma \leqq \left(-\frac{\pi}{2} + \gamma\right)$	$(\pi - \gamma) \leqq g \leqq \left(\frac{\pi}{2} - \sigma\right)$	1	0		

APPENDIX B

CHARACTERISTICS OF OPTICAL-MECHANICAL SCANNER COMPONENTS

This appendix contains typical characteristics of the components of the optical-mechanical scanner which are pertinent to this analysis. These characteristics are the transmissivity of the optics and the detectivity of the solid-state detector.

Optical Transmissivity

The optical path of the optical-mechanical scanner consists of at least one mirror and one objective lens or reflector and is assumed here to have a flat transmissivity of $\tau_{\lambda,L} = 0.7$ over the spectral range of interest. Additional filters, secondary reflectors, field lenses and/or light pipes may, of course, reduce this value.

Solid-State Detector

As indicated by the signal-to-noise ratio given by equation (28), the parameters important to this analysis are spectral detectivity and active detector area. Another parameter which is also important but less obvious is that the maximum sensitivity should occur as closely as possible to peak solar radiation. The variation of the normalized spectral detectivity D_{λ}^{*} of a silicon detector with wavelength is plotted in figure 19; the peak value is 10^{13} cm-$\sqrt{\text{Hz}}$/watt, and the diameter of the active area is 0.04 cm.

REFERENCES

1. Holter, M. R.; and Wolfe, W. L.: Optical-Mechanical Scanning Techniques. Proc. IRE, vol. 47, no. 9, Sept. 1959, pp. 1546-1550.
2. Selivanov, A. S.; Govorov, V. N.; Titov, A. S.; and Chemodanov, V. P. (Reilly Translations, transl.): Lunar Station Television Camera. NASA CR-97884, 1968.
3. Cherkasov, I. I.; Kemurdzhian, A. L.; et al.: First Panoramas of "LUNA-13" – Determination of Density and Mechanical Strength of Lunar Surface Layer at the Landing Site of the Automatic Station "LUNA-13." NASA CR-88874, 1967.
4. Bratslavets, P. F.; Rosselevich, I. A.; and Khromov, L. I.: Television Equipment for Scientific Investigations of the Cosmos. FTD-MT-24-137-67, U.S. Air Force, May 1968. (Available from DDC as AD 666071.)
5. Khodarev, Yu. K.; and Selivanov, A. S.: Space Television Systems With Mechanical Scanning. Proceedings of the Seventh International Symposium on Space Technology and Science, AGNE Pub. Inc. (Tokyo), c.1968, pp. 475-480.
6. Bratslavets, Peter Fedorovich: Television in Outer Space. JPRS 45754, U.S. Dep. Com., June 20, 1968.
7. Tompkins, D. N.: The Lunar Facsimile Camera. 1966 National Telemetering Conference Proceedings, Inst. Elec. Electron. Eng., c.1966, pp. 81-84.
8. Tompkins, Daniel N.: The Mars Facsimile Camera. AIAA/AAS Stepping Stones to Mars Meeting, Mar. 1966, pp. 14-18.
9. Wolf, E.: Light Distribution Near Focus in an Error-Free Diffraction Image. Proc. Roy. Soc. (London), ser. A, vol. 204, no. 1079, Jan. 9, 1951, pp. 533-548.
10. Born, Max; and Wolf, Emil: Principles of Optics. Third ed., Pergamon Press, c.1965.
11. Hopkins, H. H.: The Frequency Response of a Defocused Optical System. Proc. Roy. Soc. (London), ser. A, vol. 231, no. 1184, July 19, 1955, pp. 91-103.
12. Bracewell, Ron: The Fourier Transform and Its Applications. McGraw-Hill Book Co., c.1965, p. 241.
13. Fink, Donald G.: Television Engineering. Second ed., McGraw-Hill Book Co., Inc., 1952.
14. Abramowitz, Milton; and Stegun, Irene A., eds.: Handbook of Mathematical Functions With Formulas, Graphs, and Mathematical Tables. Nat. Bur. Stand., Appl. Math. Ser. 55, U.S. Dep. Com., June 1964, pp. 485, 556, 559.

15. Levi, Leo; and Austing, Richard H.; Tables of the Modulation Transfer Function of a Defocused Perfect Lens. Appl. Opt., vol. 7, no. 5, May 1968, pp. 967-974.

16. Boucher, Paul E.: Fundamentals of Photography. Third ed., D. Van Nostrand Co., Inc., c.1955, p. 57.

17. Fellgett, P. B.; and Linfoot, E. H.: On the Assessment of Optical Images. Phil. Trans. Roy. Soc., London, ser. A, vol. 247, no. 931, Feb. 17, 1955, pp. 369-407.

18. Nicodemus, Fred E.: Radiance. Amer. J. of Phys., vol. 31, no. 5, May 1963, pp. 368-377.

19. Hapke, Bruce W.: A Theoretical Photometric Function for the Lunar Surface. J. Geophys. Res., vol. 68, no. 15, Aug. 1, 1963, pp. 4571-4586.

20. Jamieson, John A.; McFee, Raymond H.; et al.: Infrared Physics and Engineering. McGraw-Hill Book Co., Inc., c.1963.

21. Oliver, B. M.; Pierce, J. R.; and Shannon, C. E.: The Philosophy of PCM. Proc. IRE, vol. 36, no. 11, Nov. 1948, pp. 1324-1331.

22. Boutry, G. A. (R. Auerbach, transl.): Instrumental Optics. Interscience Publ., Inc., 1962, p. 256.

23. Hapke, Bruce; An Improved Theoretical Lunar Photometric Function. Astron. J., vol. 71, no. 5, June 1966, pp. 333-339.

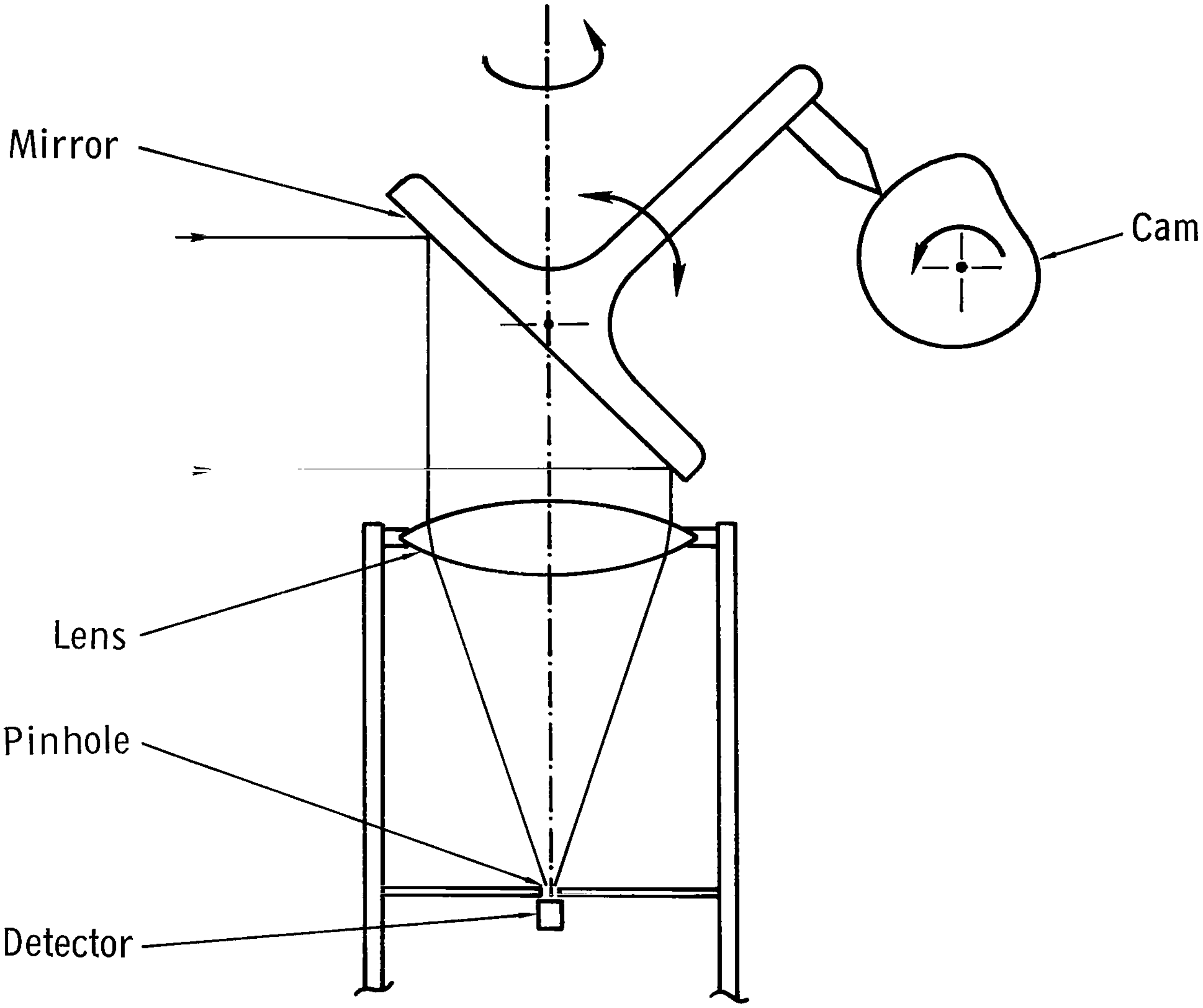

Figure 1.- A basic configuration of the optical-mechanical scanner.

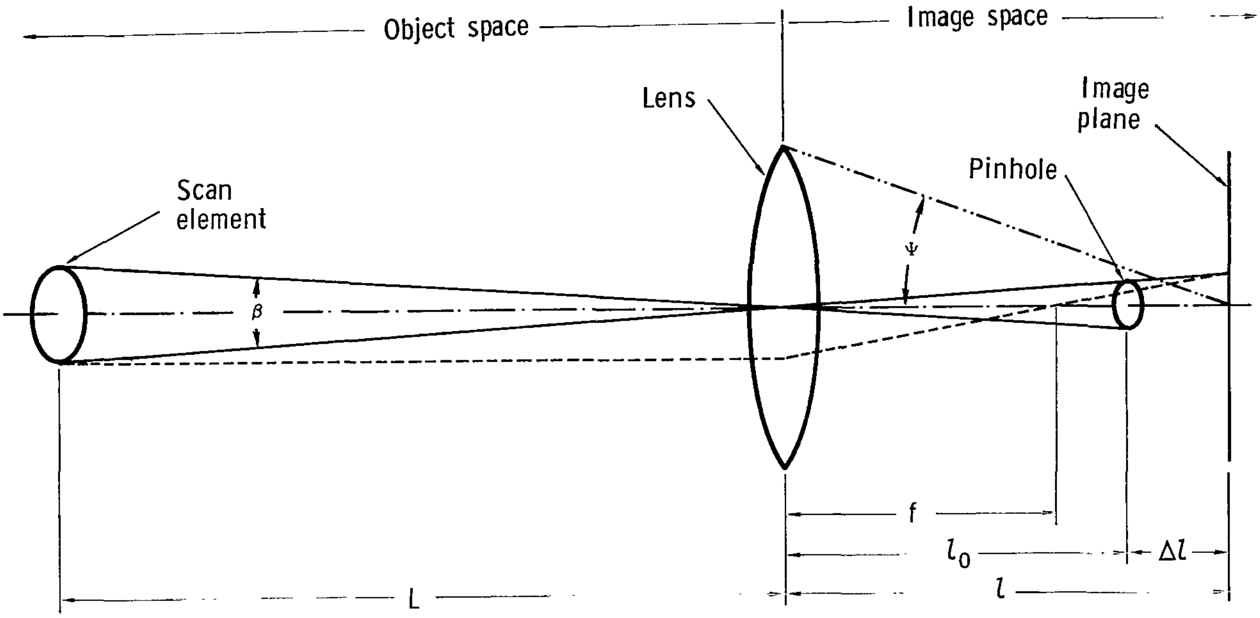

Figure 2.- Defining diagram for optical geometry.

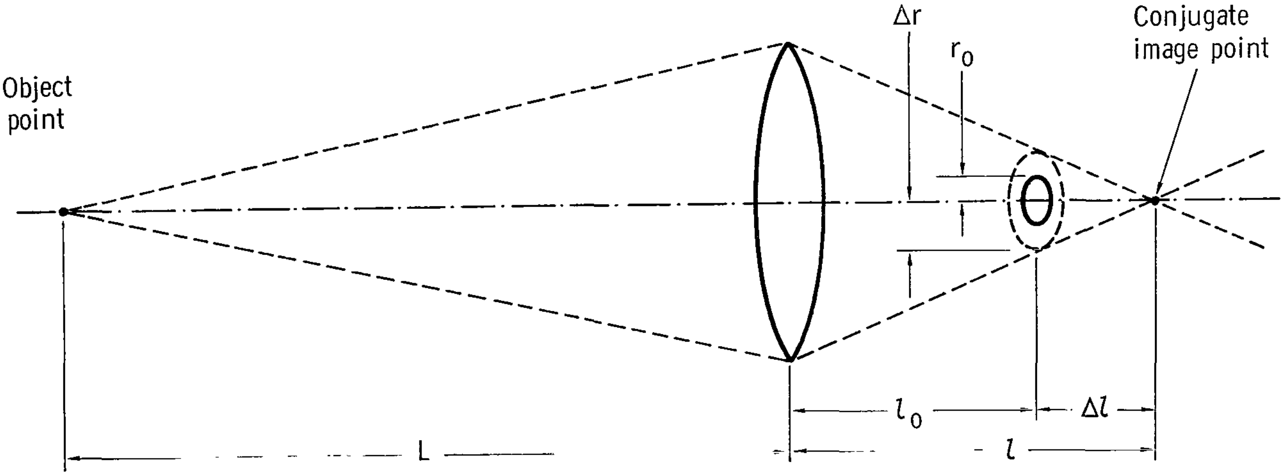

Figure 3.- Defining diagram for defect of focus.

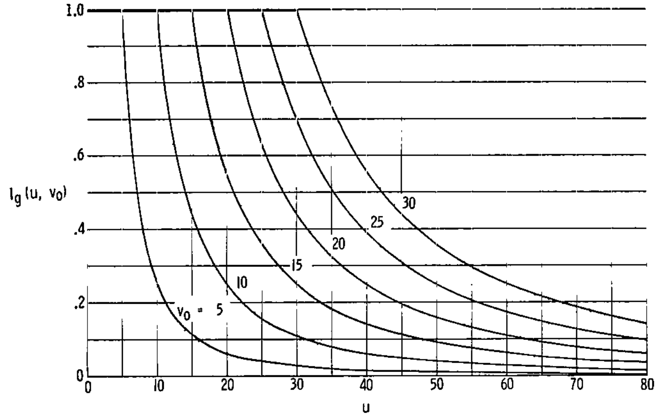

(a) Geometrical optics.

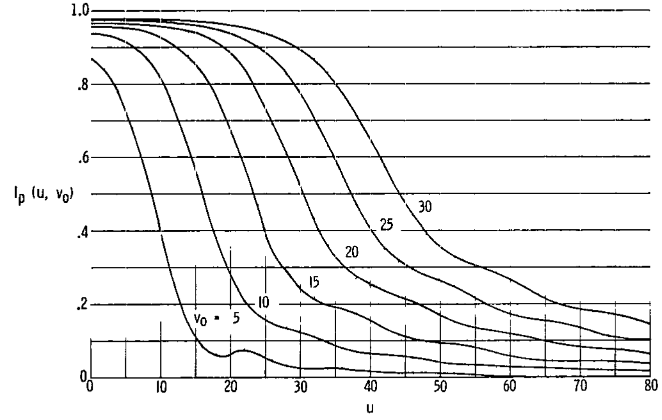

(b) Physical optics.

Figure 4.- Normalized radiation incident on a defocused pinhole from an axial object point, according to geometrical and physical optics.

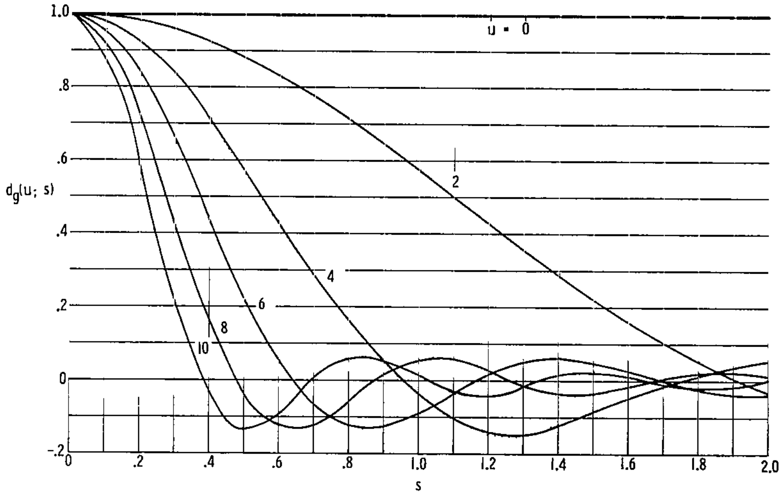

(a) Geometrical optics.

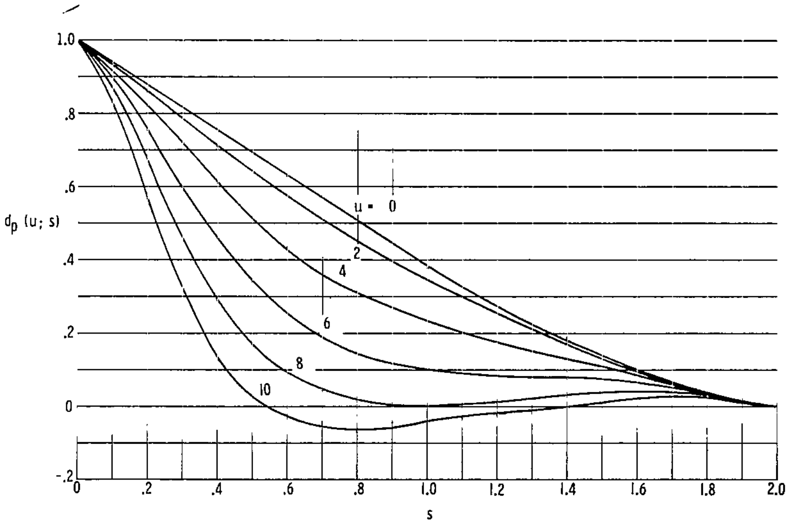

(b) Physical optics.

Figure 5.- Modulation transfer function of defocused lens, according to geometrical and physical optics.

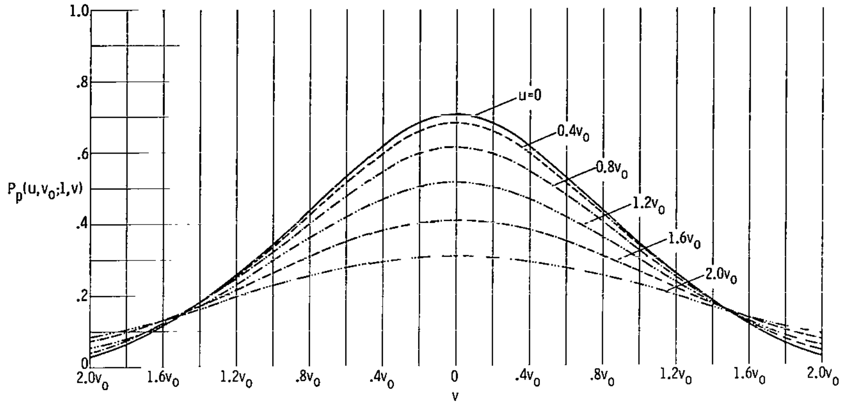

(a) $v_0 = 5$.

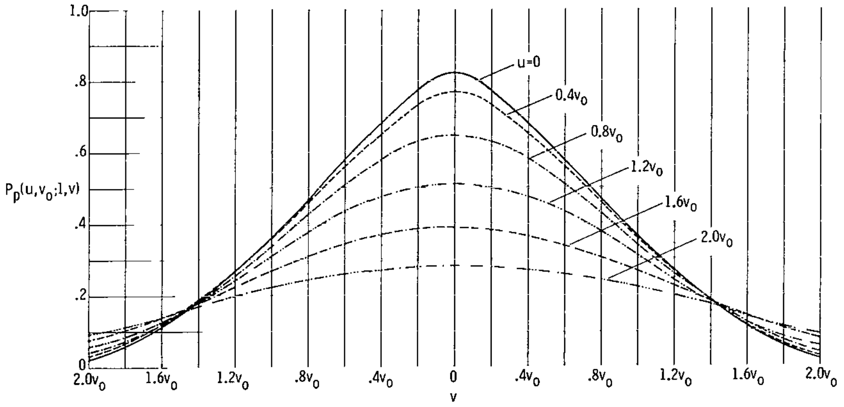

(b) $v_0 = 10$.

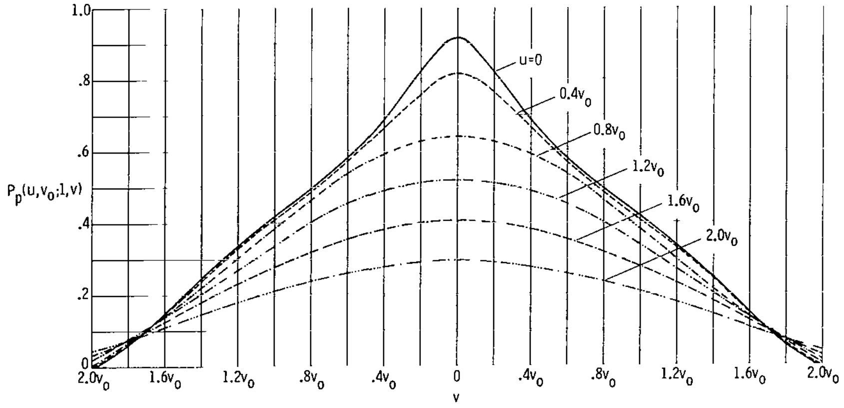

(c) $v_0 = 20$.

Figure 6.- Image distribution of a scan element for various amounts of defocus, according to physical optics.

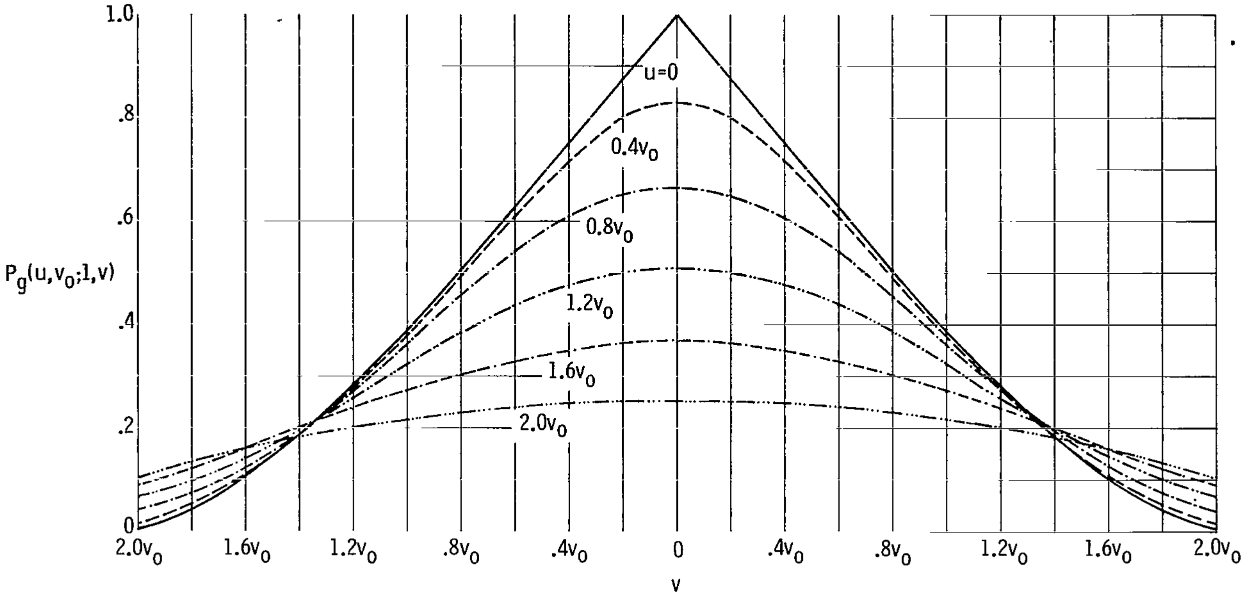

Figure 7.- Image distribution of a scan element for various amounts of defocus, according to geometrical optics.

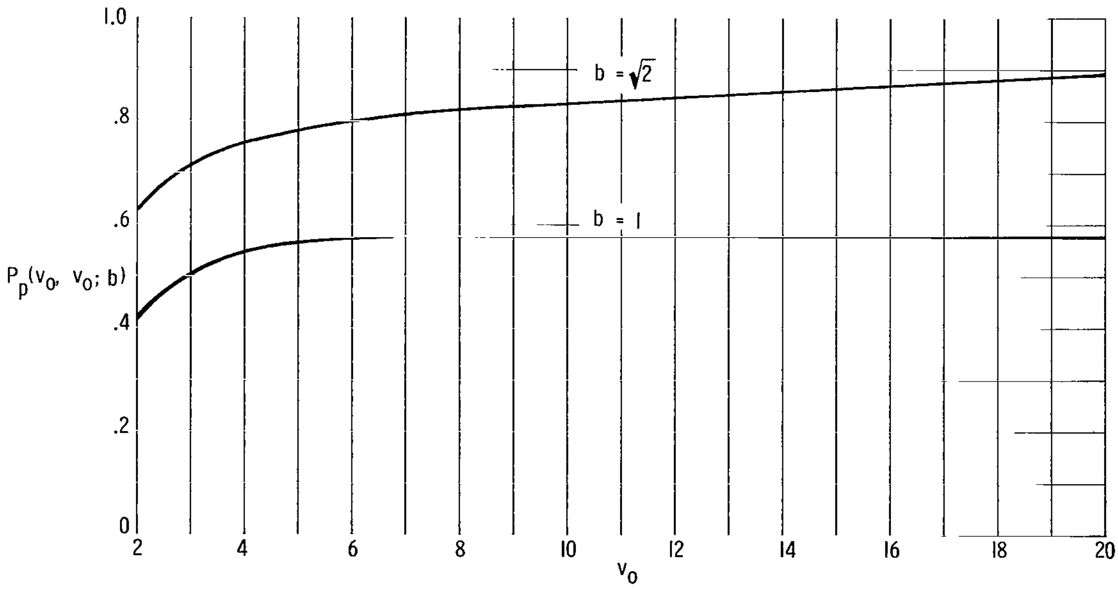

Figure 8.- Variation of peak image level of a scan and resolution element at the limits of tolerated defocus with normalized pinhole radius.

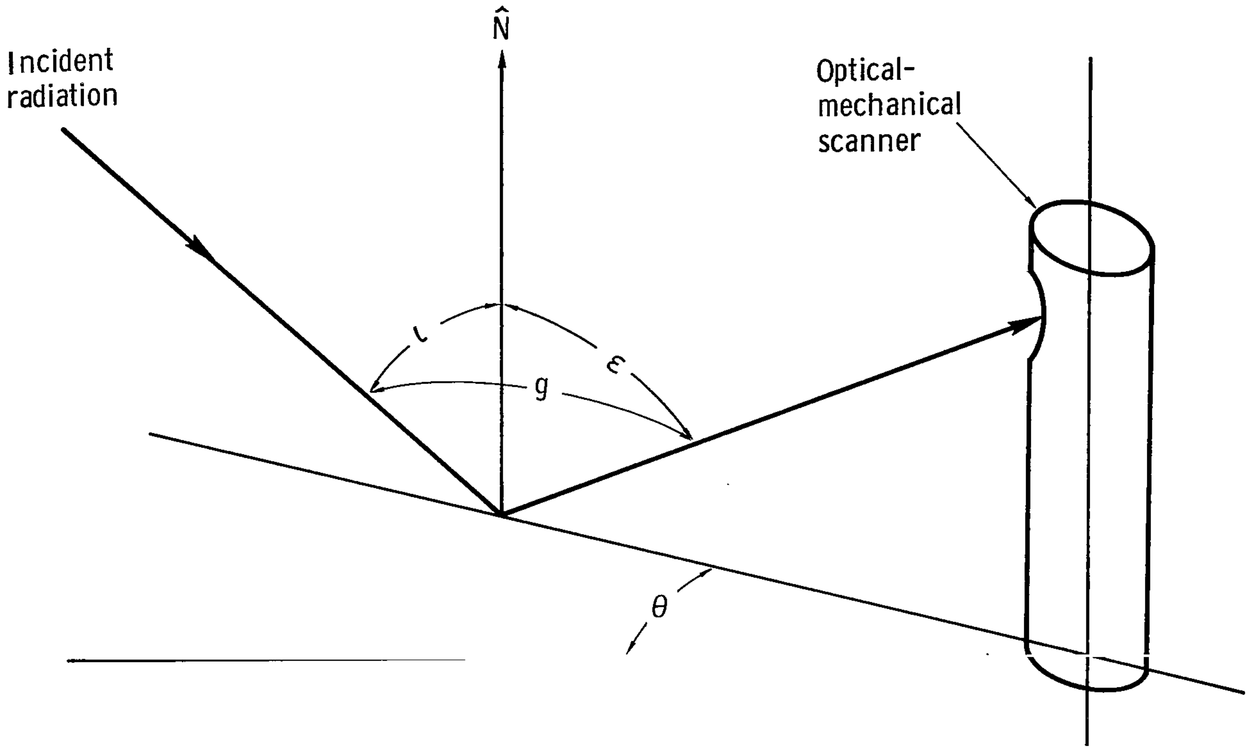

Figure 9.- Photometric angles.

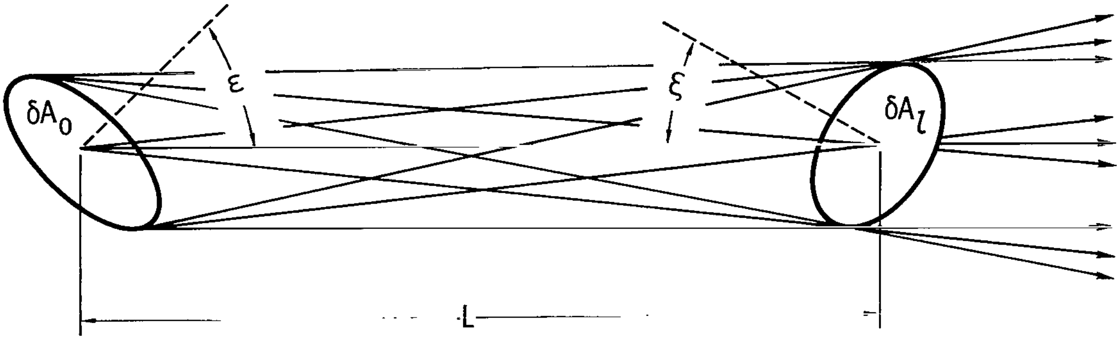

Figure 10.- Defining diagram for emitted and captured radiation.

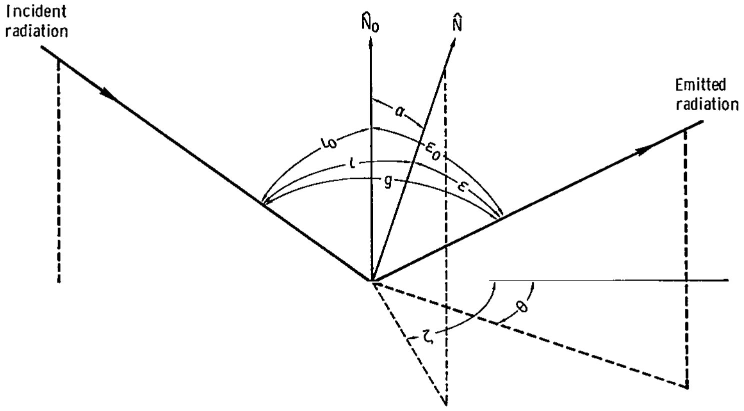

Figure 11.- Viewing geometry.

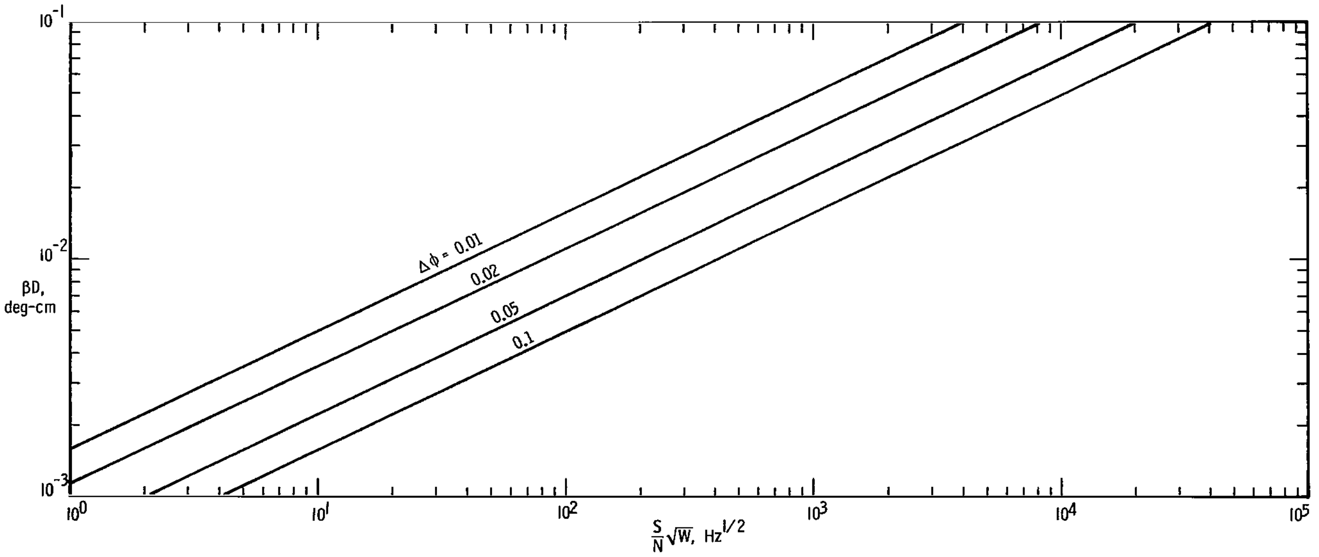

Figure 12.- Variation of βD with $\frac{S}{N}\sqrt{W}$ for several values of $\Delta\Phi$.

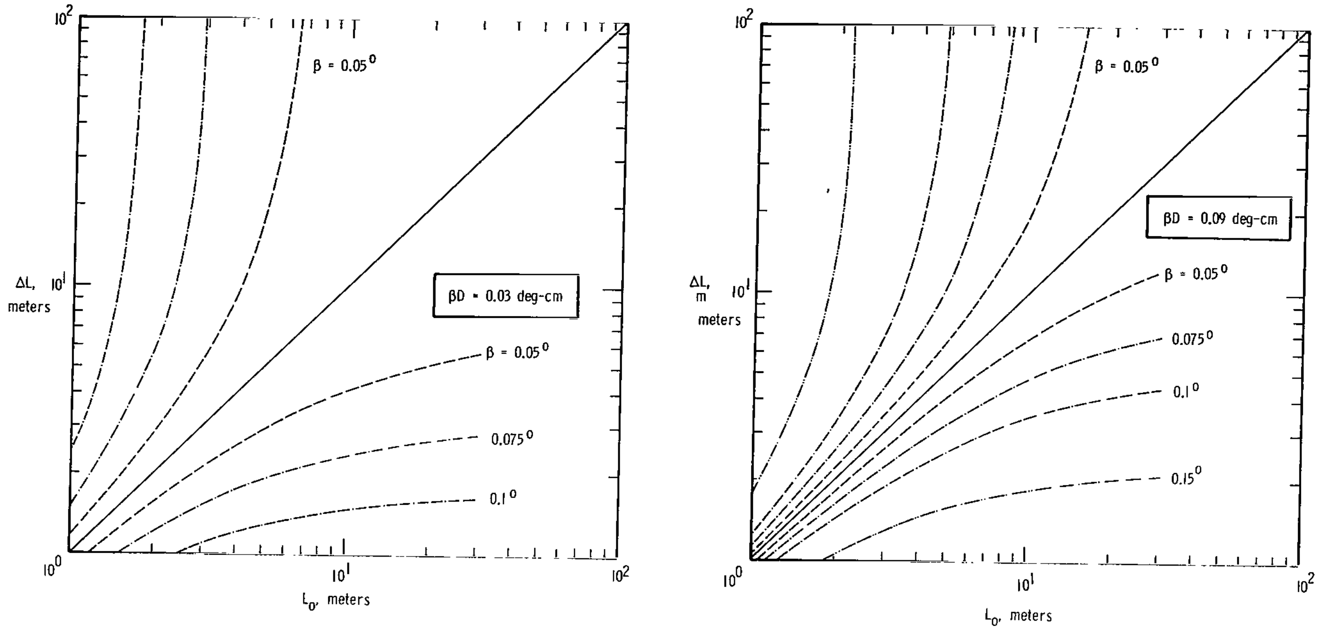

(a) Wide angular scanning resolution.

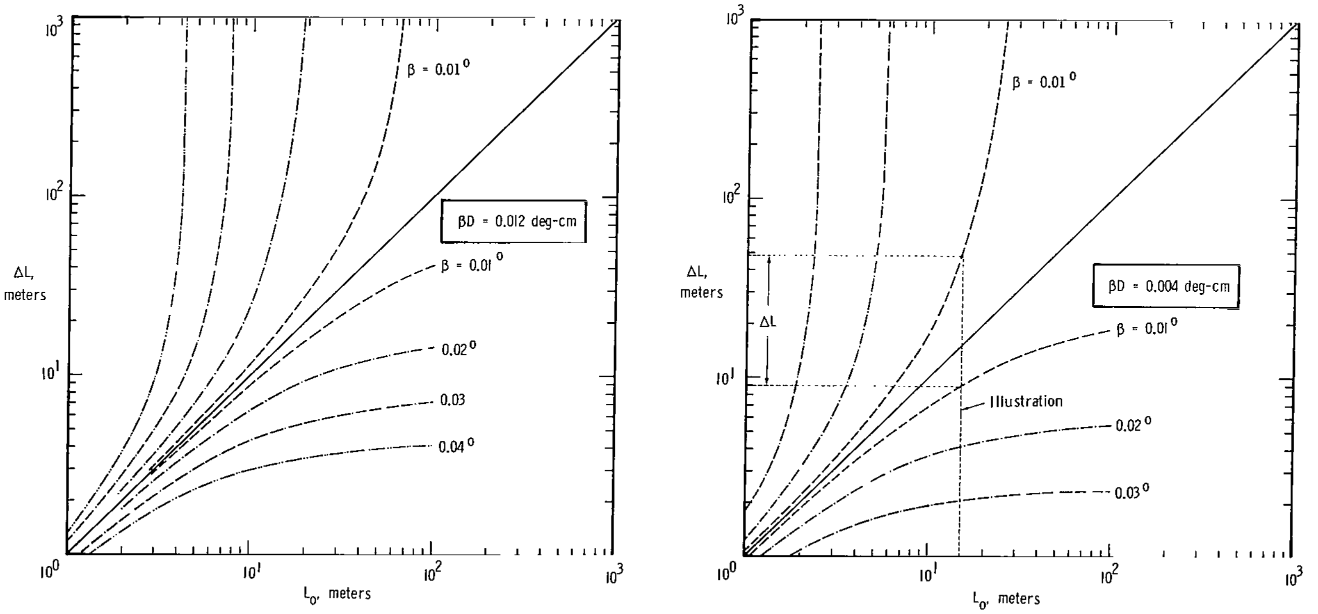

(b) Narrow angular scanning resolution.

Figure 13.- Variation of depth of field with in-focus object distance for several values of angular scanning resolution and lens diameter.

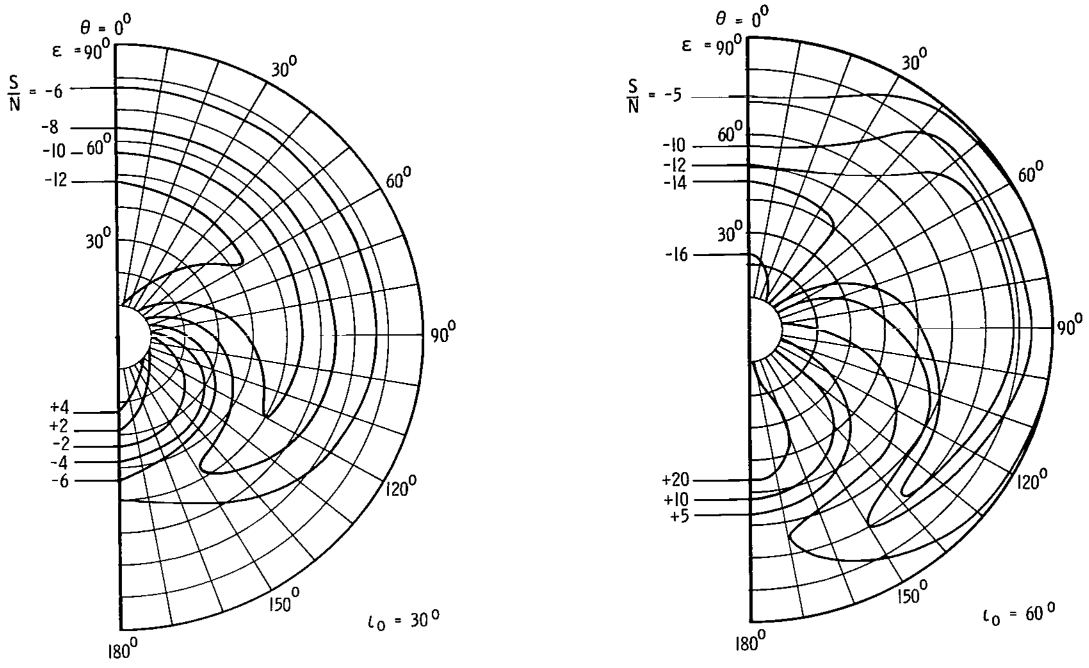

Figure 14.- Variation of the peak-signal-to-rms-noise ratio for a scan element having a slope of 6^0 and a slope azimuth of 0^0.

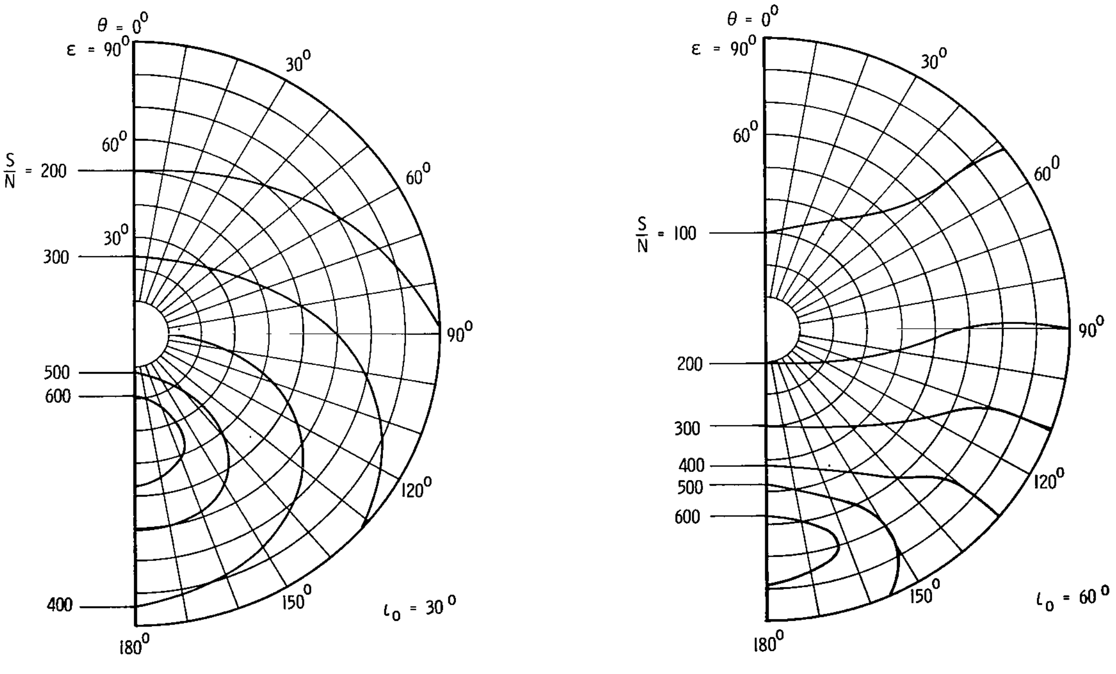

Figure 15.- Variation of the average signal-to-rms-noise ratio for a flat surface.

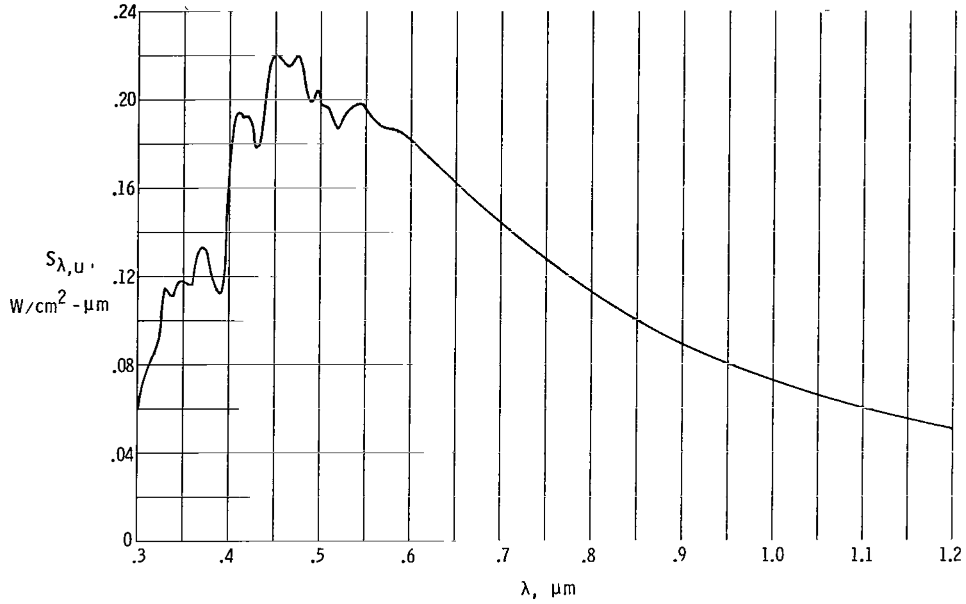

Figure 16.- Solar radiation at 1.0 astronomical unit.

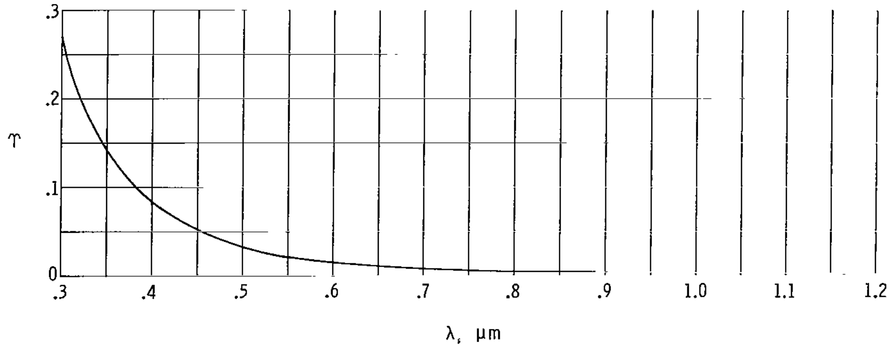

Figure 17.- Optical thickness of Martian atmosphere.

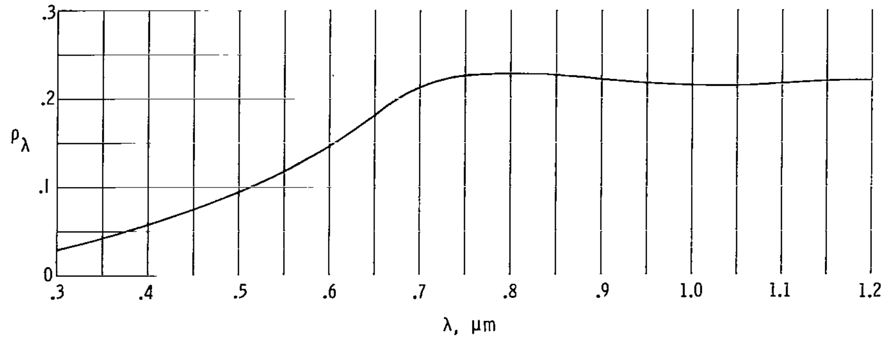

Figure 18.- Spectral reflectivity of Martian surface.

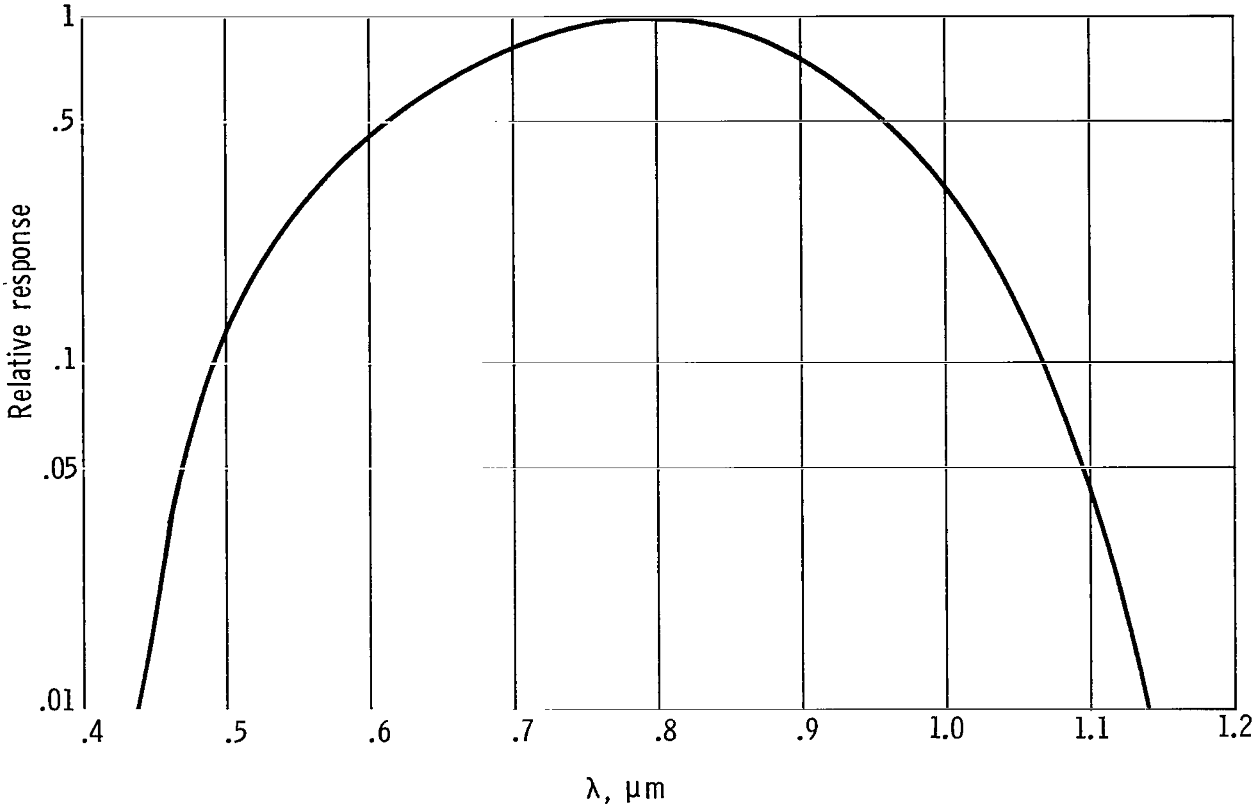

Figure 19.- Normalized spectral detectivity of a silicon detector.

NATIONAL AERONAUTICS AND SPACE ADMINISTRATION
WASHINGTON, D. C. 20546

OFFICIAL BUSINESS

FIRST CLASS MAIL

POSTAGE AND FEES PAID
NATIONAL AERONAUTICS A
SPACE ADMINISTRATION

020 001 37 51 3DS 69321 00903
AIR FORCE WEAPONS LABORATORY/WLIL/
KIRTLAND AIR FORCE BASE, NEW MEXICO 8711
ATT E. LOU BOWMAN, CHIEF, TECH. LIBRARY

POSTMASTER: If Undeliverable (Section 158
Postal Manual) Do Not Retur

> *"The aeronautical and space activities of the United States shall be conducted so as to contribute . . . to the expansion of human knowledge of phenomena in the atmosphere and space. The Administration shall provide for the widest practicable and appropriate dissemination of information concerning its activities and the results thereof."*
>
> —NATIONAL AERONAUTICS AND SPACE ACT OF 1958

NASA SCIENTIFIC AND TECHNICAL PUBLICATIONS

TECHNICAL REPORTS: Scientific and technical information considered important, complete, and a lasting contribution to existing knowledge.

TECHNICAL NOTES: Information less broad in scope but nevertheless of importance as a contribution to existing knowledge.

TECHNICAL MEMORANDUMS: Information receiving limited distribution because of preliminary data, security classification, or other reasons.

CONTRACTOR REPORTS: Scientific and technical information generated under a NASA contract or grant and considered an important contribution to existing knowledge.

TECHNICAL TRANSLATIONS: Information published in a foreign language considered to merit NASA distribution in English.

SPECIAL PUBLICATIONS: Information derived from or of value to NASA activities. Publications include conference proceedings, monographs, data compilations, handbooks, sourcebooks, and special bibliographies.

TECHNOLOGY UTILIZATION PUBLICATIONS: Information on technology used by NASA that may be of particular interest in commercial and other non-aerospace applications. Publications include Tech Briefs, Technology Utilization Reports and Notes, and Technology Surveys.

Details on the availability of these publications may be obtained from:

SCIENTIFIC AND TECHNICAL INFORMATION DIVISION
NATIONAL AERONAUTICS AND SPACE ADMINISTRATION
Washington, D.C. 20546